Biophysical control of neural trajectories under disordered brain dynamics

Matthieu Sarazin[1], David Medernach[1], Jérémie Naudé[2*], and Bruno Delord[1*]

[1] Institut des Systèmes Intelligents et de Robotique, Sorbonne Université, Centre National de la Recherche Scientifique, UMR 7222, 75005 Paris, France.

[2] Institut de Génomique Fonctionnelle, Université de Montpellier, Centre National de la Recherche Scientifique, Institut national de la santé et de la recherche médicale, UMR 5203 CNRS, rue de la Cardonille 34094 Montpellier Cedex 05, France.

[*] Equal contributions

Correspondence to

Matthieu.Sarazin@live.fr

jeremie.naude@igf.cnrs.fr

bruno.delord@gmail.com

Abstract

Neural trajectories constitute propagating sequences of activity that are essential to cognitive representations. Understanding how neural trajectories overcome the disorganizing influence of neural noise in the awake state remains challenging. Theoretical and artificial network models have focused on optimizing the synaptic pathways underlying trajectory propagation. However, in a biophysical network with synaptic plasticity, solely altering synaptic connectivity induces a tight tradeoff between spurious trajectory interruptions and inductions by noise. Formal analysis predicts that separating the inhibitory fluctuations-driven spontaneous activity from the excitatory-driven trajectory propagation is key to reliable triggering and propagation. Amongst biophysical solutions, calcium-activated suprathreshold intrinsic conductances provided the best trajectory reliability by mitigating the reliance of propagation on connectivity. These mechanisms display parametric robustness and generalize to a variety of static and dynamic attractors with uni- and bidirectional propagation. Thus, we provide a unified framework for cognitive-associated neural trajectories robust to neural noise in the awake state.

Introduction

Neural trajectories, i.e. propagating sequences of transient neural activity, represent local forms of ordered neural activity among the globally disordered activity characterizing the awake state. Neural trajectories constitute dynamical representations central to cognitive operations, from working memory to navigation across cerebral structures [1–6]. Far from simply reflecting the current sensory flow, neural trajectories can self-propagate after being initiated by a phasic stimulus cue. However, noisy spontaneous activity in the brain poses three fundamental constraints to neural trajectories.

First, noisy synaptic transmission can spuriously trigger undesired neural trajectories, affecting its *controllability*, the ability to trigger neural trajectories solely when required. Second, noise may disrupt the *stability* of activity propagation once the neural trajectory is triggered. Third, a neural trajectory could strongly modulate the activity of other neurons within local circuits, perturbing the *independence* of any other concurrent computation (e.g. multiple simultaneous independent neural trajectories). Hence, unraveling the biological mechanisms enabling reliable structured neural trajectories within noisy neural activity in cortical or subcortical structures constitutes a major goal for neuroscience.

Neural trajectories can replay offline, when sensory inputs and motor outputs are absent [4,7–9]. Learned synaptic structures within recurrent networks have thus been proposed as an underlying mechanism generating neural trajectories, which would travel along connective pathways. Theoretical studies have searched for the properties of connective pathways that could provide the highest level of controllability [10],[11]. In particular, Hebbian phase sequences, i.e. global, oriented connective pathways between Hebbian assemblies composed of locally connected neurons, can result in robust neural trajectories [10]. It is however unclear how exactly such highly complex synaptic architectures are learned. Other theoretical studies have addressed how neural trajectories embedded in noisy dynamics may emerge from training recurrent neural networks with artificial learning rules [12–14]. However, from the biophysical standpoint, a more plausible candidate for learning neural trajectory oriented connective pathways is the Spike-Timing Dependent Plasticity (STDP) rule [15]. STDP describes how pre- and postsynaptic action potentials lead to synaptic potentiation or depression, according to their temporal difference, inducing the formation of synaptic pathways [16,17].

However, how such STDP-formed connective pathways behave when embedded in a noisy recurrent network remains unknown.

Most importantly, while previous network models have been successful at identifying desirable connective pathway properties for propagating neural trajectories, they have also overlooked fundamental determinants of neuronal biophysics, such as classes of synaptic receptors or voltage- and calcium-gated conductances. Possible biological solutions to robust neural trajectories may not lie in the details of the connective pathway itself, but in the rich repertoire of neuronal properties affecting network dynamics. Hence, besides advances in the space of connective-pathway solutions, the larger space of biophysical determinants for neural trajectories has remained unexplored.

Here, we propose a dynamical and biophysical solution to both controllability, stability and independence of neural trajectories in a constrained, detailed conductance-based model of a local cortical recurrent network, with spontaneous dynamics in the asynchronous irregular regime. In this model, synaptic plasticity (STDP and synaptic scaling) leads to a diversity of neural trajectories able to express (or not) stability, controllability and independence. Neural trajectories emerged as a propagating pack of activity along the connective pathway resulting from strong associative NMDA excitatory deterministic transmission at high firing frequencies. This mechanism contrasted with spontaneous AI activity, which was based on inhibitory GABA-A fluctuations at low firing frequencies. Using theoretical analysis, we characterized a firing frequency threshold separating spontaneous and pack propagation regimes, pointing at mechanisms increasing the separation between these regimes, as key factors for trajectory controllability and stability. We then identified three classes of biophysical processes increasing such separation: low inhibitory fluctuations, strong tonic feedforward inhibition and excitatory recurrent connectivity, as well as calcium-dependent suprathreshold afterhyperpolarization and afterdepolarization intrinsic currents. The latter mechanism – which could not have been predicted by approaches optimizing the connective pathway – proved the most efficient at stability and controllability. Moreover, it also granted the largest independence between the neural trajectory and surrounding network activity, by mitigating the reliance of activity propagation on synaptic properties only. These results proved robust to model parameters and generalized to a wide spectrum of static, dynamic, discrete and continuous neural trajectories, subserving a wide array of representations. Altogether, we thus unveil a generic principle (the dual

stochastic/deterministic dynamical regime) with an efficient biophysical solution (spike-triggered currents) for the learning and expression of neural trajectories robust to the neural noise encountered in the physiological conditions of cognitive operations.

Results

Robust STDP-induced neural trajectories in the asynchronous irregular (AI) regime

We designed a detailed, physiologically-constrained biophysical recurrent neural network model accounting for the highly irregular activity of cortical structures (**Fig. 1a**, see *Methods*). Neuronal activity displayed low frequencies (**Fig. 1b**, $\nu < 10Hz$, **Fig. S1a**, [18]), irregularity (inter-spike intervals (ISIs) $CV \sim 1$ and $CV_2 \sim 0.8$, **Fig. S1b-d**, [19]) and asynchrony (average pairwise correlation $< \rho > \sim 0.01$, **Fig. S1e-g**, [20]) characteristic of the asynchronous irregular (AI) regime [21], typical in behaving mammals [22]. The corresponding chaotic dynamics ($\lambda \sim 0.01$, **Fig. S1h-j**, [23]) emerged from fluctuation-based spiking (**Fig. 1c** top) due to the balanced, strong total current generated by excitatory and inhibitory inputs (**Fig. 1c** bottom, and **Fig. S1k**, [24]), i.e. neurons were in the high-conductance state [25].

We evaluated the ability of the network to learn connective pathways through activity-dependent synaptic plasticity. The network was trained with a circular trajectory stimulus (**Fig. 1d**, left) inducing biophysically plausible Spike-Timing Dependent Plasticity (STDP) and synaptic scaling, which are ubiquitous in the neocortex (see *Methods*, [26,27]). Synapses were potentiated when postsynaptic followed presynaptic spikes (**Fig. 1d**, center**)**. Thus, sequential neuronal activation potentiated synapses connecting neurons that were activated in the forward direction along the trajectory, forming an oriented "*connective pathway"* that constituted an engram of the stimulus (arrows, **Fig. 1d**, right). Synaptic scaling homeostatically compensated for Hebbian plasticity run-away by regulating the sum of incoming weights onto neurons [26,28]. Incoming weights sums were thus similar across neurons (**Fig. 1d**, right), while the oriented connective pathway arose from the direction in which outgoing weights were most potentiated.

We next evaluated whether the resulting connective pathway could propagate a "*pack"*, defined as the set of co-active spiking neurons among the trajectory. Expression of neural trajectories in the presence of chaotic synaptic fluctuations is far from trivial: noise may disrupt packs at any moment, forbidding faithful propagation, thus requiring a sufficiently strong connective pathway. However, strong weights may ignite packs in an uncontrolled fashion from a few spikes in trajectory neurons. Furthermore, packs may propagate and perturb concurrent computations outside the trajectory, e.g. other simultaneous independent neural trajectories. Indeed, after learning, synchronized excitatory spiking rapidly amplified along the connective pathway, recruiting more neurons and converging to

a propagation state implying ~100 neurons, affecting global network dynamics (**Fig. 1e-h**).

Strikingly, the same network architecture yielded diverse neural trajectories, depending on the realization of random connectivity before learning, or initial activity conditions, due to chaotic dynamics. Neural trajectories could emerge spontaneously (**Fig. 1e**, **1g**) or when triggered by an initiating stimulus (red rectangle, **Fig. 1f**, **1h**). The trajectory could spontaneously, stably and permanently express, possibly overwhelming network dynamics (**Fig. 1e**). On the other hand, neural trajectories could fail to propagate stably, due to noise fluctuations (**Fig. 1f**). Nevertheless, neural trajectories could also account for physiological observations **(Fig. 1g-h**), i.e. sparse spontaneous trajectories (e.g. free replay, **Fig. 1g**) or stable evoked-only trajectories (e.g. correct GO task performance, **Fig. 1h**). Thus, biologically plausible STDP can train recurrent networks to express neural trajectories in the presence of neural noise, while not systematically granting their functionality. To understand how functional trajectories emerge, we assessed the dynamical regimes determining whether activity packs propagate or not.

Pack propagation relies on the transition from inhibitory fluctuation- to excitatory mean current-driven spiking

To unravel the mechanisms underlying pack propagation, we first identified the causes of spiking in excitatory situated within a propagating pack (*"pack neurons*") or outside ("*non-pack neurons"*).

In *non-Pack* neurons, the membrane potential reached a sub-threshold steady-state plateau (~54mV, **Fig. 2a**, top left), as the total current was essentially near-balanced on average (**Fig. 2b**, top left, star). Spiking arose from fast voltage transients (**Fig. 2a**, top left, star) caused by strong current fluctuations (**Fig. 2b**, bottom left, star). $GABA_A$ fluctuations contributed the most among synaptic currents (**Fig. 2b**, bottom middle, star), spiking being mostly caused by sudden $GABA_A$ transient decreases (**Fig. 2a**, bottom left, star). Spiking in *non-Pack* neurons was thus mostly driven by disinhibitory fluctuations.

In *pack* neurons, the potential rose to threshold without an intermediate plateau (**Fig. 2a**, top right), because a strongly imbalanced depolarizing total current (**Fig. 2b**, top left, triangle) resulted from a strong tonic NMDA drive (**Fig. 2b**, top right, triangle, and **Fig. 3a**, right). This drive was particularly massive due to 1) strong spiking frequency (f_{Pack}~$14.5Hz$), 2) large potentiated synaptic weights within the connective pathway, and 3) pre-/post-

coincident spiking relieving Mg^{2+}-mediated NMDA blockade and inducing associative NMDA activation. Moreover, the local excitatory pack only slightly activated inhibitory neurons (**Fig. 1h**), because inhibition was global (non-specific synapses to and from inhibitory neurons), which further contributed to the total current imbalance.

Thus, while spontaneous activity was fundamentally GABA-A-fluctuation-based in the low-frequency spontaneous global AI regime, pack propagation along the connective pathway rather relied on local, deterministic and associative NMDA transmission at higher frequencies. We next assessed the mechanisms setting transitions between these regimes, to understand the conditions for the emergence and extinction of neural trajectories.

Theoretical analysis of transitions between spontaneous activity and pack propagation

Characterizing transitions first required identifying the frontier separating activity regimes. Both regimes differed by their firing frequency (f), which determined the mean magnitude and fluctuations of synaptic currents responsible for activity (see above). To assess the complex interactions at work in a tractable framework, we determined the frequency threshold separating regimes (**Fig. 3a**) in a reduced (one-dimensional) analytical model investigating the conditions allowing for propagation of activity between preceding and succeeding neurons along the trajectory pathway, as a function of f (see *Methods*). This *propagation threshold theory* predicted that the frequency threshold f_θ separated activity regimes in excitatory neurons (**Fig. 3a**, left) was an unstable fixed-point, with self-amplifying activity above and extinction below. The theory closely replicated average currents in spontaneous vs propagation regimes in the network model (**Fig. 3a**, right); as well as the threshold value itself ($f_\theta \sim 10.2Hz$ – vs $f_\theta \sim 9.2Hz$ in network simulations, see *Methods*). Based on this propagation threshold, we designed a *regime transition theory* (**Fig. 3b**, see *Methods*) predicting noise-driven transitions between activity regimes. This theory described firing frequency dynamics through a differential equation accounting for stable fixed-points characterizing both regimes ($f_{non-Pack}$ and f_{Pack}), the separating unstable threshold f_θ (**Fig. 3b**, left), and a stochastic component accounting for noise-driven frequency fluctuations and subsequent regime transitions (**Fig. 3b**, right), whose standard deviations $\sigma_{non-Pack}$ and σ_{Pack} were estimated from network simulations.

This theory allowed to compute the probabilities of spontaneous $p(Spont.)$ and triggered $p(Evoked)$ transitions toward pack propagation. Subsequently, we defined the

controllability of neural trajectories as ($p(Evoked) - (Spont.)$) to quantify the ability for reliable stimulus, but limited spontaneous, triggering of trajectories. The stability of trajectories was computed as the duration of evoked pack propagation (see *Methods*). Low levels or variability of firing frequency in the spontaneous regime ($f_{non-Pack}$ or $\sigma_{non-Pack}$) decreased $p(Spont.)$ but had no influence on $p(Evoked)$, increasing controllability (**Fig. 3c**, first two panels). Conversely, in the propagation regime, larger firing frequency (f_{Pack}) or lower frequency variability (σ_{Pack}) increased $p(Evoked)$, but had no influence on $p(Spont.)$, increasing controllability (**Fig. 3c**, third and fourth panels). Finally, controllability displayed an optimum as a function of f_θ (as it decreased p($Spont.$) first, and then p($Evoked$), **Fig. 3c**, last panel).

Altogether, the theory predicted that biophysical factors promoting a larger separation between regimes (larger distance to frequency threshold or lower frequency variability) should increase controllability, while stability should increase with factors limiting downward transitions from the propagation regime (i.e. higher f_{Pack} or lower σ_{Pack}, **Fig. 3c**, third and fourth panels).

Biophysical mechanisms promoting stability and controllability

These theoretical predictions led us to investigate the biophysical determinants of propagation in network simulations. When conducting extensive parametric explorations to find biophysical determinants allowing a clear separation between activity regimes, i.e. ensuring both stability and controllability, we identified a restricted set of architectural, synaptic and ionic possible candidates.

The straightforward solution of strengthening the connective pathway (i.e. by increasing STDP amplitude A_{STDP}) enhanced stability, due to a higher pack frequency (**Fig. 4a**, left). However, it also increased the probability of spontaneous packs, due to a decreased f_θ (**Fig. 4a**, left), thus having a limited impact upon controllability (**Fig. 4a**, middle). By contrast, we devised that decreasing inhibitory current fluctuations onto excitatory neurons (while keeping their mean constant) should reduce $f_{non-Pack}$ and $p(Spont.)$ – by rendering disinhibition scarce. This should thus separate the two regimes, as the spontaneous regime was mostly disinhibitory-driven, while the evoked regime was not. A larger number of proportionally weaker $I \rightarrow E$ synapses (higher $p_{I\rightarrow E}$, see *Methods*) was used to decrease $GABA_A$ current fluctuations ($\sigma(I_{GABA-A})$, **Fig. S2a**, top). As predicted, lower $\sigma(I_{GABA-A})$

decreased $f_{non-Pack}$ (and thus $\sigma_{non-Pack}$, **Fig. 4b**, left) and $p(Spont.)$ (**Fig. 4b**, middle), leading to more controllability. Stability was also increased: f_{pack} increased because the decreased $f_{non-Pack}$ lowered the excitatory drive to inhibitory neurons, which, in turn, decreased the inhibitory drive on pack neurons. Alternatively, slower but proportionally weaker GABA-A currents could also reduce inhibitory current fluctuations, with similar effects (**Fig. S2a**, bottom and **Fig. S2b**).

Combining tonic feedforward inhibition with stronger recurrent excitatory connectivity also increased controllability and stability. Indeed, stronger excitatory recurrence (e.g. strengthened STDP, $A_{STDP} = 75$) increased f_{Pack} and decreased f_{θ} without modifying $f_{non-Pack}$ (**Fig. 4c**, left, black vertical line vs. **Fig. 4a**, left, black vertical line), as previously shown. This resulted in greater separation between f_{Pack} and $f_{non-Pack}$, although $f_{non-Pack}$ was now much closer to f_{θ}, inducing high $p(Spont.)$ at low $\nu_{FF(Inh)}$ (**Fig. 4c**, left and middle). Therefore, we also increased feedforward tonic inhibition (i.e. $\nu_{FF(Inh)}$), which decreased $f_{non-Pack}$ and f_{Pack} by the same amount (while keeping f_{θ} relatively constant, **Fig. 4c**, left), thus decreasing both $p(Spont.)$ and $p(Evoked)$. The net effects were a higher f_{Pack} and lower $f_{non-Pack}$, resulting in higher controllability and stability within an intermediate $\nu_{FF(Inh)}$ range, although $p(Evoked)$ and controllability eventually decreased at high $\nu_{FF(Inh)}$. Intuitively, this mechanism could be understood as favoring inhibition independent of network frequency in order to decrease spontaneous firing frequency and neural trajectories likelihood, while simultaneously increasing network-dependent excitation for higher evoked frequency and neural trajectories probability. Favoring frequency-independent hyperpolarizing currents on excitatory neurons could be achieved in many other ways with similar effects, reinforcing its validity as a general principle ensuring stability and controllability in real recurrent neural networks. For instance, decreasing the hyperpolarizing leak current of inhibitory neurons ($g_{L(Inh)}$), or decreasing recurrent currents impinging upon inhibitory neurons ($g_{X\to I}$), in order to obtain higher inhibitory frequency in the spontaneous regime, led to similar effects (**Fig. S2c-d**).

Besides synaptic and architectural parameters, we discovered that calcium-activated, suprathreshold, non-specific cationic (CAN) and after-hyperpolarization potassium (AHP) ionic currents were major determinants of controllability and stability. Both currents depend upon spike-driven calcium influx, through voltage-dependent calcium channels, and, thus, on spiking frequency. Specifically, the combination of a slow AHP saturating at low spike

frequency and a fast CAN saturating at high spike frequency induced hyperpolarization at low firing frequencies (due to AHP) and depolarization at high frequencies (due to CAN) (**Fig. 4e**, left). In individual neurons, CAN and AHP together entailed an unstable fixed point at f'_θ~12.7Hz (**Fig. 4e**, left), with AHP favoring activity extinction below f'_θ, preventing unwanted neural trajectories, while CAN favored self-amplifying activity above f'_θ, stabilizing evoked trajectories. This cellular mechanism boosted the separation between regimes at the network level, with decreased $f_{non-pack}$ and increased f_{pack} (**Fig. 4d**, left), increasing controllability and stability (**Fig. 4d**, middle). Noticeably, this effect did not require strong conductances promoting absolute intrinsic bistability (i.e. persistent activity), as a weak CAN conductance, yielding transient bistability, sufficed to promote controllability and stability of neural trajectories (**Fig. 4e**, middle).

Independence between trajectory and surrounding activity

Generally, increasing controllability and stability required decreasing spontaneous network activity. However, in such conditions, completion of the neural trajectory increased the frequency of excitatory (and inhibitory) neurons that were not part of the trajectory, creating a sharp contrast between background network dynamics outside and during neural trajectories (**Fig. 4b-d**, right). Such strong modulation of the whole network activity might impede upon parallel concurrent computations, e.g. simultaneous distinct trajectories. We assessed which mechanisms enabled the best network *independence*, i.e. produced less perturbation of neural dynamics outside the trajectory. To do so, we computed an independence measure $I = 1 - \left|\frac{f_{nT(Ev.)} - f_{nT(Sp.)}}{f_{nT(Ev.)} + f_{nT(Sp.)}}\right|$, with $f_{nT}(Ev.)$ and $f_{nT}(Sp.)$ representing the frequency of excitatory neurons outside the trajectory during pack propagation and during the spontaneous regime, respectively (**Fig. 4a-d**, middle). $I = 1$ corresponds to equal frequencies, decreasing I to increasingly different frequencies, and $I = 0$ to either frequency being null. Increasing controllability and stability generally decreased independence (down to ~50%, from a ~90% baseline). However, independence decreased less with the CAN/AHP mechanism (to ~70%), having an excitatory component increasing the spontaneous excitatory frequency (g_{CAN}). This result pinpointed the beneficial computational influence of interacting synaptic (connective pathway) and intrinsic (CAN-AHP) properties, as already noticed before [29]. Indeed, CAN-AHP led to transient bistability within neurons (**Fig. 4e**,

middle and right), which lessened the burden resting on synaptic properties with regard to pack propagation.

Robustness of reliable neural trajectories within the AI regime

We assessed whether the identified mechanisms were robust to the biophysical variability found across cerebral structures and species, in order to assess their biological plausibility and genericity. We thus evaluated the width of parameter regions allowing trajectory reliability (controllability, stability and independence), while preserving asynchronous irregular network dynamics, by systematically varying parameters for each of the aforementioned mechanisms (see *Methods* and **Fig. S3a-c**). In the standard model (i.e. devoid of any mechanism improving trajectory reliability, model ∅), controllable and stable trajectories emerged for moderately large parametric regions (overall robustness ~10%). By contrast, we found much larger regions with the aforementioned additional mechanisms (~25%), peaking with the CAN-AHP mechanism (~45%, **Fig. 4f**, left). More specifically, although the $\nu_{FF(Inh)}$ mechanism resulted in the largest parametric regions allowing for controllability and stability (when evaluated individually), the parametric width for independence decreased with $\sigma(I_{GABA-A})$ and $\nu_{FF(Inh)}$ (~60%), compared to the model ∅. However, it remained at ~100% with CAN-AHP, allowing for independent concurrent computations outside the trajectory, and further supporting intrinsic currents as plausible generic candidates alleviating constraints on synaptic-based propagation (**Fig. 4f**, right).

A common framework for generalized static and dynamical neural attractors

Beyond robustness, genericity lies in the functional versatility of neural representations supported by these aforementioned architectural, synaptic and intrinsic mechanisms. Indeed, networks endowed with one or several of these mechanisms could learn synaptic structures responsible for a large repertoire of attractors, from discrete static (Hebbian assemblies) to dynamic (synfire chain and Hebbian phase sequence) attractors, as well as continuous static (ring-like) and dynamic (bidirectional ring) attractors (**Fig. 5a**). Learning such structures required varying stimulus properties and the asymmetry and shift of the STDP window (**Fig. 5b**), as observed across different cerebral structures [27] or neuromodulatory states (e.g. dopamine, [30]).

Symmetric STDP rules (**Fig. 5c1-2**, second panel), combined with discrete stimuli,

formed discrete static attractors. Exposure to a single discrete stimulus (**Fig. 5c1**, first panel) led to the formation of a Hebbian assembly (HA, **Fig. 5c1**, third panel). Combined with the CAN/AHP mechanism, a stimulus triggered self-sustained activity in the HA, with increased reliability (vs model ∅, **Fig. 5c1**, fourth panel). Similarly, a stimulus jumping between successive discrete positions (**Fig. 5c2**, first panel) formed multiple HAs (**Fig. 5c2**, third panel), which could be independently selected and expressed with increased reliability via the added CAN-AHP mechanism (vs model ∅, **Fig. 5c2**, fourth panel).

By contrast, asymmetric STDP rules combined with discrete stimuli led to discrete dynamical attractors. A discretely moving stimulus (**Fig. 5d1**, first panel), with a strongly asymmetric and shifted STDP window (**Fig. 5d1**, second panel), led to the learning (**Fig. 5d1**, third panel) of a synfire chain, with fast reliable traveling of spiking across neuronal groups ($\sigma(I_{GABA-A})$ and $\nu_{FF(Inh)}$ mechanisms, **Fig. 5d1**, fourth panel). The same stimulus (**Fig. 5d2**, first panel), learned through a weakly asymmetric STDP window (**Fig. 5d2**, second panel) led to HAs connected through feedforward connections (**Fig. 5d2**, third panel) and the expression of a Hebbian phase sequence, i.e. successive slow (few hundred ms) recalls of HAs ($\sigma(I_{GABA-A})$ mechanism, **Fig. 5d2**, fourth panel).

Besides, a continuously moving stimulus (**Fig. 5e1**, first panel) with a symmetric STDP window (**Fig. 5e1**, second panel) led to a ring-like attractor (**Fig. 5e1**, third panel) supporting multiple simultaneous trajectories and extremely slow drift across time (CAN-AHP mechanism, **Fig. 5e1**, fourth panel). Finally, the same stimulus (**Fig. 5e2**, first panel), with a larger STDP window (**Fig. 5e2**, second panel) resulted in a ring attractor with a larger symmetrical connective pathway (**Fig. 5e2**, third panel), which allowed bidirectional trajectory expression in the direction of the initial moving stimulus when combined with slowly-saturating g_{AHP} (see *Methods*, $\sigma(I_{GABA-A})$ mechanism, **Fig. 5e2**, fourth panel).

Altogether, these results suggest that the mechanisms we have identified represent generic computational processes allowing controllable and stable expression of a wide array of dynamical representations that have been proposed for cognitive functions.

Discussion

Using simulations and theoretical analyses of biophysically-constrained network models, we showed how interactions between intrinsic and synaptic properties of recurrent neural networks grant a large set of functionally reliable, robust and generic attractor dynamics including neural trajectories, despite the permanent disorganizing effects of neural noise under the chaotic asynchronous irregular (AI) dynamics characterizing wakefulness.

STDP learning of neural trajectories in the AI regime

Despite the generic prevalence and functional significance of neural trajectories in many cognitive operations [5,8,9,31,32], theoretical models have underexplored the mechanisms underlying their functional emergence and propagation under the jeopardizing asynchronous irregular (AI) dynamics encountered during awake cognition. While Spike-Timing Dependent Plasticity (STDP)-based learning is considered a natural candidate for learning neural trajectories, STDP-based models have not assessed trajectory reliability under neural noise [16,17]. In others, plasticity is either absent [10], based on artificial (non-local) learning rules [12–14] or the AI regime of neuronal activity is lacking [33,34]. Compared to existing models, here we operationalized the problematic in terms of stability, controllability and independence of evoked trajectories. This allowed us to assess biophysical mechanisms as possible determinants of functional trajectory.

Biophysics of reliable trajectories goes beyond synaptic connectivity

Similar to larger issues in computational neurosciences [35], network models have focused on synaptic connectivity for propagating trajectories, but have overlooked the rich repertoire of neuronal biophysics (e.g. synaptic receptors or intrinsic conductances). Thus, the immense space of biophysical determinants for neural trajectories has remained underexplored, despite advances in the subspace of connective solutions. Yet, biophysical determinants have been evolutionarily selected for their ability to confer real neural circuits with efficient computational solutions to dynamical cognitive demands.

We found generic trends: biophysical determinants promoting a larger separation between spontaneous and propagation regimes (larger frequency distance to threshold,

lower frequency variability) increased trajectory controllability while those limiting downward transitions from propagation to spontaneous activity (i.e. higher mean and lower variability of pack frequency) increased stability. This allowed the identification of precise biophysical substrates for neural trajectories, amenable to experimental investigation. Consistent with its known role in the maintenance of working memory (Hebbian static attractor, [36]), slow NMDA dynamics increased the reliability of trajectory propagation (dynamic attractor). We further revealed how fast GABA-A currents, which are necessary for high-conductance state characterizing AI dynamics [21], are central in setting spontaneous, inhibitory fluctuations-driven spiking, and thus in preventing unwanted initiation of spontaneous trajectories. We predict that manipulations of GABA-A time constant, by preserving global inhibitory drive but perturbing inhibitory fluctuations, should affect spontaneous replays. Several classes of mechanisms were based on inhibition, either through decreasing disinhibitory GABA-A fluctuations or combining tonic frequency-independent inhibition with stronger recurrent excitatory connectivity. This last possibility is reminiscent of mediodorsal thalamic activation, which increases fast spiking firing frequency and amplifies local regular spiking functional connectivity in rodent mPFC, promoting stable sparse transient neural sequences and working memory performance [6]. Overall, our framework may be useful for the understanding of pathological dynamics. For instance, schizophrenia is characterized by both unwanted spontaneous activity and unstable attractors, pointing at the biophysical determinants of the separation between spontaneous activity and neural trajectories as substrates of interest [37].

Noticeably, we found that frequency-dependent CAN/AHP ionic currents yielded the best combination of controllability, stability, independence and robustness, offering the best compromise, among all tested possibilities, regarding the tradeoff between increased controllability and stability and decreased independence. We thus suggest spike-triggered calcium-dependent ionic channels as substrates of interest for schizophrenia studies.

Altogether, these results pointed to the biophysical plausibility and potential genericity of mechanisms based on calcium-dependent currents in promoting reliable replays across cerebral structures, since these currents are ubiquitous [29]. Moreover, this possibility is appealing, since interactions between synaptic and intrinsic properties alleviate the burden resting on connectivity concerning the generation of neural trajectories. Such a solution, based on intrinsic properties, could not have been predicted by approaches optimizing the

connective pathway, in particular the popular artificial training of neural networks.

Genericity of the model

Using the biophysical mechanisms identified, together with different STDP windows and stimuli, allowed to control the expression of a large spectrum of known attractors, from discrete static (Hebbian assemblies) or dynamic (synfire chains and Hebbian phase sequences) attractors, to continuous static (ring-like) and dynamic (bidirectional ring) attractors. Dynamic attractors could be reliably expressed, escaping the classical issue of propagation failure or of uncontrolled sequential propagation [10,38]. Continuous static (ring-like) attractors presented virtually null levels of drift, a standard issue encountered in current models [39]. Finally, continuous dynamic attractors allowed bidirectional propagation of neural trajectories, which is novel without a complex setup and arbitrary synaptic matrices [10]. Such STDP diversity has been observed experimentally across neural structure or neuromodulatory states [27,30]. Noticeably, Figure 5 provides a set of non-trivial predictions linking the shape of the STDP window (to be observed in a given cellular type) to the dynamical properties of the neural trajectories that brain structures produce.

Functionality of physiological neural trajectories

Here, we considered spontaneous trajectories as diminishing trajectory controllability. However, functionally-relevant spontaneous replays occur physiologically in cortical and hippocampal networks when animals consolidate learnt behaviors during sleep [40–42], evaluate past and future behavioral choices or rules [4,7–9], or link different sequences [43]. However, they are scarce and may become physiologically detrimental when incessant or overwhelming. We found spontaneous replays to be trivially obtained in a large domain of the network biophysical state space (e.g. strong STDP), highlighting the importance of mechanisms limiting the probability of spontaneous trajectory initiation. This constraint becomes crucial in contexts where trajectories must be reliably evoked only when triggered. Regarding stability, stable neural trajectories are not systematically required, as in the case of transient dynamics [44]. However, stable neural trajectories clearly represent a strategic advantage for cognitive operations such as navigation, or dynamical coding during working memory, which require reliable execution over seconds to minutes [5,32,45–48]. Although not studied *per se*, evidence suggests approximate independence of neural trajectory and network activity in

cortical and subcortical structures [2,5,8,49,50], which makes sense given the crucial importance of co-existing parallel cognitive operations or alternative evaluations of behavioral choices. We thus provide clear testable predictions on the level of independence expected in neural structures, and on plausible biophysical substrates of interest – spike-triggered calcium-dependent currents – for further experimental and theoretical investigation. A related avenue of future research would require evaluating whether the mechanisms identified here allow independent replay of multiple trajectories in the same network, depending on their degree of overlap.

References

1. Fujisawa, S., Amarasingham, A., Harrison, M. T. & Buzsáki, G. Behavior-dependent short-term assembly dynamics in the medial prefrontal cortex. *Nat. Neurosci.* **11**, 823–833 (2008).
2. Harvey, C. D., Coen, P. & Tank, D. W. Choice-specific sequences in parietal cortex during a virtual-navigation decision task. *Nature* **484**, 62–68 (2012).
3. Hussar, C. R. & Pasternak, T. Memory-Guided Sensory Comparisons in the Prefrontal Cortex: Contribution of Putative Pyramidal Cells and Interneurons. *J. Neurosci.* **32**, 2747–2761 (2012).
4. Pfeiffer, B. E. & Foster, D. J. Hippocampal place-cell sequences depict future paths to remembered goals. *Nature* **497**, 74–79 (2013).
5. Yang, S.-T., Shi, Y., Wang, Q., Peng, J.-Y. & Li, B.-M. Neuronal representation of working memory in the medial prefrontal cortex of rats. *Mol. Brain* **7**, 61 (2014).
6. Rikhye, R. V., Gilra, A. & Halassa, M. M. Thalamic regulation of switching between cortical representations enables cognitive flexibility. *Nat. Neurosci.* **21**, 1753–1763 (2018).
7. Diba, K. & Buzsáki, G. Forward and reverse hippocampal place-cell sequences during ripples. *Nat. Neurosci.* **10**, 1241–1242 (2007).
8. Jadhav, S. P., Rothschild, G., Roumis, D. K. & Frank, L. M. Coordinated Excitation and Inhibition of Prefrontal Ensembles during Awake Hippocampal Sharp-Wave Ripple Events. *Neuron* **90**, 113–127 (2016).
9. Kaefer, K., Nardin, M., Blahna, K. & Csicsvari, J. Replay of Behavioral Sequences in the Medial Prefrontal Cortex during Rule Switching. *Neuron* (2020) doi:10.1016/j.neuron.2020.01.015.
10. Chenkov, N., Sprekeler, H. & Kempter, R. Memory replay in balanced recurrent networks. *PLoS Comput. Biol.* **13**, (2017).
11. Pereira, U. & Brunel, N. Unsupervised Learning of Persistent and Sequential Activity. *Front. Comput. Neurosci.* **13**, (2020).
12. Sussillo, D. & Abbott, L. F. Generating Coherent Patterns of Activity from Chaotic Neural Networks. *Neuron* **63**, 544–557 (2009).
13. Laje, R. & Buonomano, D. V. Robust timing and motor patterns by taming chaos in recurrent neural networks. *Nat. Neurosci.* **16**, 925–933 (2013).
14. Xue, X., Halassa, M. M. & Chen, Z. S. Spiking recurrent neural networks represent task-relevant neural sequences in rule-dependent computation. *bioRxiv* 2021.01.21.427464 (2021) doi:10.1101/2021.01.21.427464.
15. Bi, G. Q. & Poo, M. M. Synaptic modifications in cultured hippocampal neurons: dependence on spike timing, synaptic strength, and postsynaptic cell type. *J. Neurosci. Off. J. Soc. Neurosci.* **18**, 10464–10472 (1998).
16. Hayashi, H. & Igarashi, J. LTD windows of the STDP learning rule and synaptic connections having a large transmission delay enable robust sequence learning amid background noise. *Cogn. Neurodyn.* **3**, 119–130 (2009).
17. Clopath, C., Büsing, L., Vasilaki, E. & Gerstner, W. Connectivity reflects coding: a model of voltage-based STDP with homeostasis. *Nat. Neurosci.* **13**, 344–352 (2010).
18. Boudewijns, Z. S. R. M. *et al.* Layer-specific high-frequency action potential spiking in the prefrontal cortex of awake rats. *Front. Cell. Neurosci.* **7**, (2013).
19. Compte, A. Temporally Irregular Mnemonic Persistent Activity in Prefrontal Neurons of Monkeys During a Delayed Response Task. *J. Neurophysiol.* **90**, 3441–3454 (2003).

20. Tchumatchenko, T., Geisel, T., Volgushev, M. & Wolf, F. Signatures of synchrony in pairwise count correlations. *Front. Comput. Neurosci.* **4**, (2010).
21. Brunel, N. Dynamics of Sparsely Connected Networks of Excitatory and Inhibitory Spiking Neurons. *J. Comput. Neurosci.* **8**, 183–208 (2000).
22. Poulet, J. F. A. & Petersen, C. C. H. Internal brain state regulates membrane potential synchrony in barrel cortex of behaving mice. *Nature* **454**, 881–885 (2008).
23. London, M., Roth, A., Beeren, L., Häusser, M. & Latham, P. E. Sensitivity to perturbations in vivo implies high noise and suggests rate coding in cortex. *Nature* **466**, 123–127 (2010).
24. Xue, M., Atallah, B. V. & Scanziani, M. Equalizing excitation–inhibition ratios across visual cortical neurons. *Nature* **511**, 596–600 (2014).
25. Destexhe, A., Rudolph, M. & Paré, D. The high-conductance state of neocortical neurons *in vivo*. *Nat. Rev. Neurosci.* **4**, 739–751 (2003).
26. Turrigiano, G. G., Leslie, K. R., Desai, N. S., Rutherford, L. C. & Nelson, S. B. Activity-dependent scaling of quantal amplitude in neocortical neurons. *Nature* **391**, 892–896 (1998).
27. Abbott, L. F. & Nelson, S. B. Synaptic plasticity: taming the beast. *Nat. Neurosci.* **3**, 1178–1183 (2000).
28. Sarazin, M. X. B., Victor, J., Medernach, D., Naudé, J. & Delord, B. Online Learning and Memory of Neural Trajectory Replays for Prefrontal Persistent and Dynamic Representations in the Irregular Asynchronous State. *Front. Neural Circuits* **0**, (2021).
29. Rodriguez, G. *et al.* Conditional bistability, a generic cellular mnemonic mechanism for robust and flexible working memory computations. *J. Neurosci.* 1992–17 (2018) doi:10.1523/JNEUROSCI.1992-17.2017.
30. Zhang, J.-C., Lau, P.-M. & Bi, G.-Q. Gain in sensitivity and loss in temporal contrast of STDP by dopaminergic modulation at hippocampal synapses. *Proc. Natl. Acad. Sci.* **106**, 13028–13033 (2009).
31. Batuev, A. S. Two neuronal systems involved in short-term spatial memory in monkeys. *Acta Neurobiol. Exp. (Warsz.)* **54**, 335–344 (1994).
32. Schmitt, L. I. *et al.* Thalamic amplification of cortical connectivity sustains attentional control. *Nature* **545**, 219–223 (2017).
33. Liu, J. K. & Buonomano, D. V. Embedding Multiple Trajectories in Simulated Recurrent Neural Networks in a Self-Organizing Manner. *J. Neurosci.* **29**, 13172–13181 (2009).
34. Fiete, I. R., Senn, W., Wang, C. Z. H. & Hahnloser, R. H. R. Spike-Time-Dependent Plasticity and Heterosynaptic Competition Organize Networks to Produce Long Scale-Free Sequences of Neural Activity. *Neuron* **65**, 563–576 (2010).
35. Saxe, A., Nelli, S. & Summerfield, C. If deep learning is the answer, what is the question? *Nat. Rev. Neurosci.* **22**, 55–67 (2021).
36. Wang, X.-J. Synaptic Basis of Cortical Persistent Activity: the Importance of NMDA Receptors to Working Memory. *J. Neurosci.* **19**, 9587–9603 (1999).
37. Rolls, E. T. & Deco, G. A computational neuroscience approach to schizophrenia and its onset. *Neurosci. Biobehav. Rev.* **35**, 1644–1653 (2011).
38. Mehring, C., Hehl, U., Kubo, M., Diesmann, M. & Aertsen, A. Activity dynamics and propagation of synchronous spiking in locally connected random networks. *Biol. Cybern.* **88**, 395–408 (2003).
39. Seeholzer, A., Deger, M. & Gerstner, W. Stability of working memory in continuous attractor networks under the control of short-term plasticity. *PLOS Comput. Biol.* **15**, e1006928 (2019).
40. Lee, A. K. & Wilson, M. A. Memory of Sequential Experience in the Hippocampus

during Slow Wave Sleep. *Neuron* **36**, 1183–1194 (2002).
41. Euston, D. R., Tatsuno, M. & McNaughton, B. L. Fast-Forward Playback of Recent Memory Sequences in Prefrontal Cortex During Sleep. *Science* **318**, 1147–1150 (2007).
42. Girardeau, G., Benchenane, K., Wiener, S. I., Buzsáki, G. & Zugaro, M. B. Selective suppression of hippocampal ripples impairs spatial memory. *Nat. Neurosci.* **12**, 1222–1223 (2009).
43. Buzsáki, G. & Moser, E. I. Memory, navigation and theta rhythm in the hippocampal-entorhinal system. *Nat. Neurosci.* **16**, 130–138 (2013).
44. Durstewitz, D. & Deco, G. Computational significance of transient dynamics in cortical networks. *Eur. J. Neurosci.* **27**, 217–227 (2008).
45. Sreenivasan, K. K., Curtis, C. E. & D'Esposito, M. Revisiting the role of persistent neural activity during working memory. *Trends Cogn. Sci.* **18**, 82–89 (2014).
46. Mello, G. B. M., Soares, S. & Paton, J. J. A Scalable Population Code for Time in the Striatum. *Curr. Biol.* **25**, 1113–1122 (2015).
47. Bolkan, S. S. *et al.* Thalamic projections sustain prefrontal activity during working memory maintenance. *Nat. Neurosci.* **20**, 987–996 (2017).
48. Spaak, E., Watanabe, K., Funahashi, S. & Stokes, M. G. Stable and Dynamic Coding for Working Memory in Primate Prefrontal Cortex. *J. Neurosci.* **37**, 6503–6516 (2017).
49. Pastalkova, E., Itskov, V., Amarasingham, A. & Buzsaki, G. Internally Generated Cell Assembly Sequences in the Rat Hippocampus. *Science* **321**, 1322–1327 (2008).
50. Cromer, J. A., Roy, J. E. & Miller, E. K. Representation of Multiple, Independent Categories in the Primate Prefrontal Cortex. *Neuron* **66**, 796–807 (2010).
51. Dale, H. Pharmacology and Nerve-endings (Walter Ernest Dixon Memorial Lecture): (Section of Therapeutics and Pharmacology). *Proc. R. Soc. Med.* **28**, 319–332 (1935).
52. Beaulieu, C., Kisvarday, Z., Somogyi, P., Cynader, M. & Cowey, A. Quantitative distribution of gaba-immunopositive and -immunonegative neurons and synapses in the monkey striate cortex (area 17). *Cereb. Cortex* **2**, 295–309 (1992).
53. Thomson, A. M. Synaptic Connections and Small Circuits Involving Excitatory and Inhibitory Neurons in Layers 2-5 of Adult Rat and Cat Neocortex: Triple Intracellular Recordings and Biocytin Labelling In Vitro. *Cereb. Cortex* **12**, 936–953 (2002).
54. Song, S., Sjöström, P. J., Reigl, M., Nelson, S. & Chklovskii, D. B. Highly Nonrandom Features of Synaptic Connectivity in Local Cortical Circuits. *PLOS Biol.* **3**, e68 (2005).
55. Haj-Dahmane, S. & Andrade, R. Calcium-Activated Cation Nonselective Current Contributes to the Fast Afterdepolarization in Rat Prefrontal Cortex Neurons. *J. Neurophysiol.* **78**, 1983–1989 (1997).
56. Villalobos, C., Shakkottai, V. G., Chandy, K. G., Michelhaugh, S. K. & Andrade, R. SKCa Channels Mediate the Medium But Not the Slow Calcium-Activated Afterhyperpolarization in Cortical Neurons. *J. Neurosci.* **24**, 3537–3542 (2004).
57. Faber, E. L. & Sah, P. Functions of Sk Channels in Central Neurons. *Clin. Exp. Pharmacol. Physiol.* **34**, 1077–1083 (2007).
58. Brunel, N. & Wang, X. J. Effects of neuromodulation in a cortical network model of object working memory dominated by recurrent inhibition. *J. Comput. Neurosci.* **11**, 63–85 (2001).
59. Jahr, C. E. & Stevens, C. F. Voltage dependence of NMDA-activated macroscopic conductances predicted by single-channel kinetics. *J. Neurosci.* **10**, 3178–3182 (1990).
60. Wang, H., Stradtman, G. G., Wang, X.-J. & Gao, W.-J. A specialized NMDA receptor function in layer 5 recurrent microcircuitry of the adult rat prefrontal cortex. *Proc. Natl. Acad. Sci.* (2008) doi:10.1073/pnas.0804318105.

61. Destexhe, A., Mainen, Z. F. & Sejnowski, T. J. Kinetic models of synaptic transmission. *Methods Neuronal Model.* **2**, 1–25 (1998).
62. Wolf, A., Swift, J., Swinney, H. & Vastano, J. Determining Lyapunov exponents from a time series. *Phys. Nonlinear Phenom.* 285–317 (1985).
63. Huffaker, R. Phase Space Reconstruction from Econommic Time Series Data: Improving Models of Complex Real-World Dynamic Systems. *Int. J. Food Syst. Dyn.* **1**, 184–193 (2010).
64. Kliková, B. & Raidl, A. Reconstruction of Phase Space of Dynamical Systems Using Method of Time Delay. *Proc. 20th Annu. Conf. Dr. Stud. - WDS 2011* 83–87 (2011).
65. Kantz, H. & Schreiber, T. *Nonlinear Time Series Analysis*. (Cambridge University Press, 2004).
66. Kennel, M. B., Brown, R. & Abarbanel, H. D. I. Determining embedding dimension for phase-space reconstruction using a geometrical construction. *Phys. Rev. A* **45**, 3403–3411 (1992).
67. Hegger, R. & Kantz, H. Improved false nearest neighbor method to detect determinism in time series data. *Phys. Rev. E Stat. Phys. Plasmas Fluids Relat. Interdiscip. Top.* **60**, 4970–4973 (1999).
68. Shinomoto, S., Miyazaki, Y., Tamura, H. & Fujita, I. Regional and Laminar Differences in In Vivo Firing Patterns of Primate Cortical Neurons. *J. Neurophysiol.* **94**, 567–575 (2005).
69. Golomb, D., Hansel, D. & Mato, G. Chapter 21 Mechanisms of synchrony of neural activity in large networks. in *Handbook of Biological Physics* (eds. Moss, F. & Gielen, S.) vol. 4 887–968 (North-Holland, 2001).

Author contributions

MS JN BD designed the model and research project. MS DM BD simulated the model and analyzed its behavior. MS JN BD wrote the article.

Figures and Figure legends

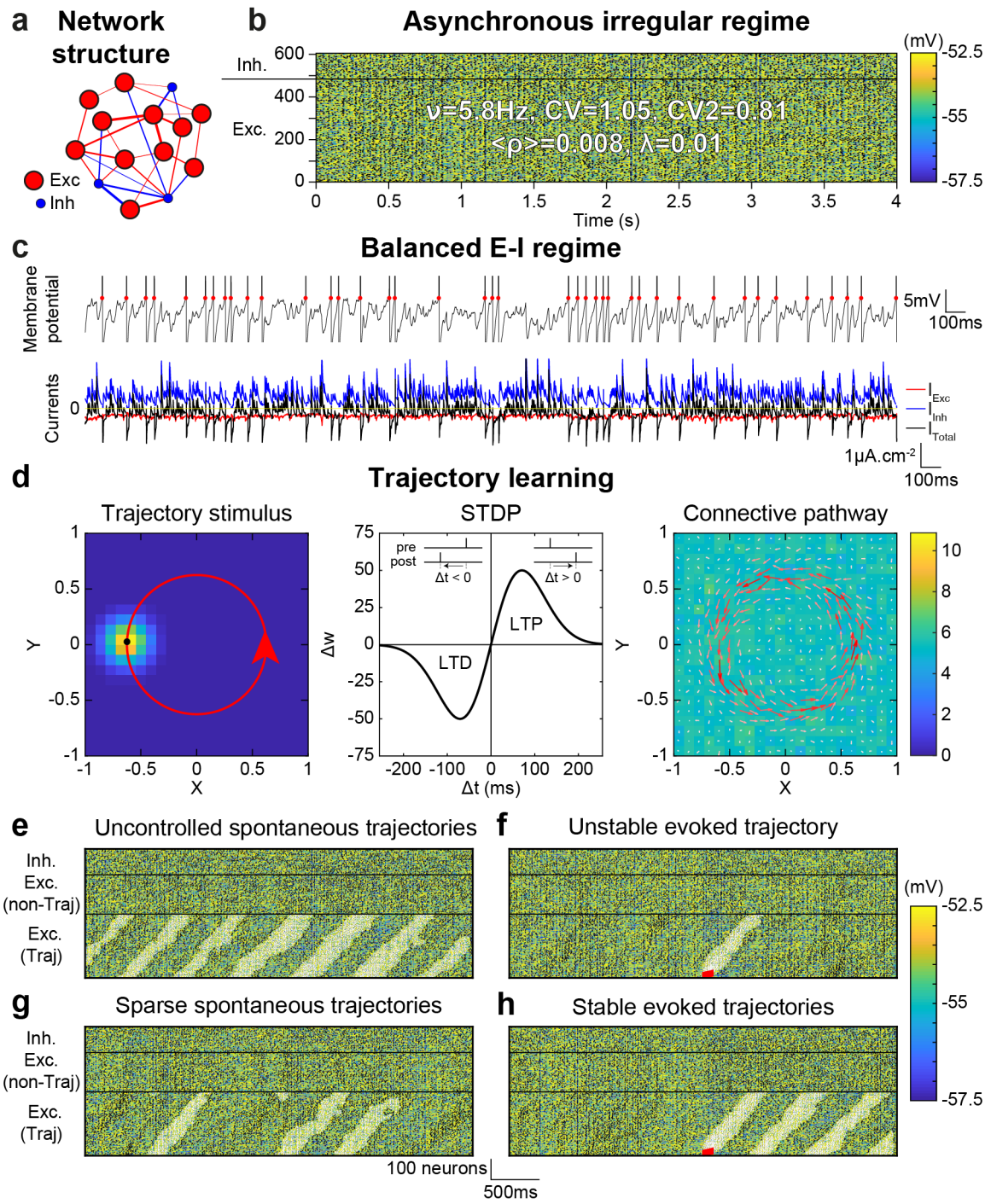

Figure 1. STDP-induced trajectory replay diversity within the balanced AI regime. (**a**) Randomly connected recurrent neural network of 80% excitatory and 20% inhibitory neurons (14 neurons are shown, whereas the model is composed of 605 neurons, i.e. 484 excitatory, 121 inhibitory). (**b**) Asynchronous irregular network activity, with spikes (black dots) and membrane potential of neurons across 4 seconds of simulation. (**c**) Subthreshold membrane potential and irregular spikes (top) driven by current fluctuations, since excitatory and inhibitory currents are balanced on average (bottom). (**d**)

(Left) External circular trajectory stimulus (red circle), activating neurons through putative spatially-organized receptive fields. Example activity of neurons (background colors) induced by the trajectory stimulus at a given time point (black dot). (Middle) Temporal window of the STDP learning rule, inducing LTP for positive time differences (pre- then post-synaptic spikes) and LTD for negative time differences (post- then pre-synaptic spikes). (Right) Resulting connective pathway, with normalized arrows showing the direction in which outgoing weights are most potentiated (white to red arrow color scheme with increasing arrow magnitude), and homogeneous background colors showing similar sums of total incoming weights onto neurons (due to synaptic scaling) (**e-h**) Resulting connective pathways induce a variety of different trajectory replays, which emerge spontaneously (**e** & **g**) or can be evoked via a strong stimulus onto the first 25 neurons of the trajectory (red rectangle, **f** & **h**).

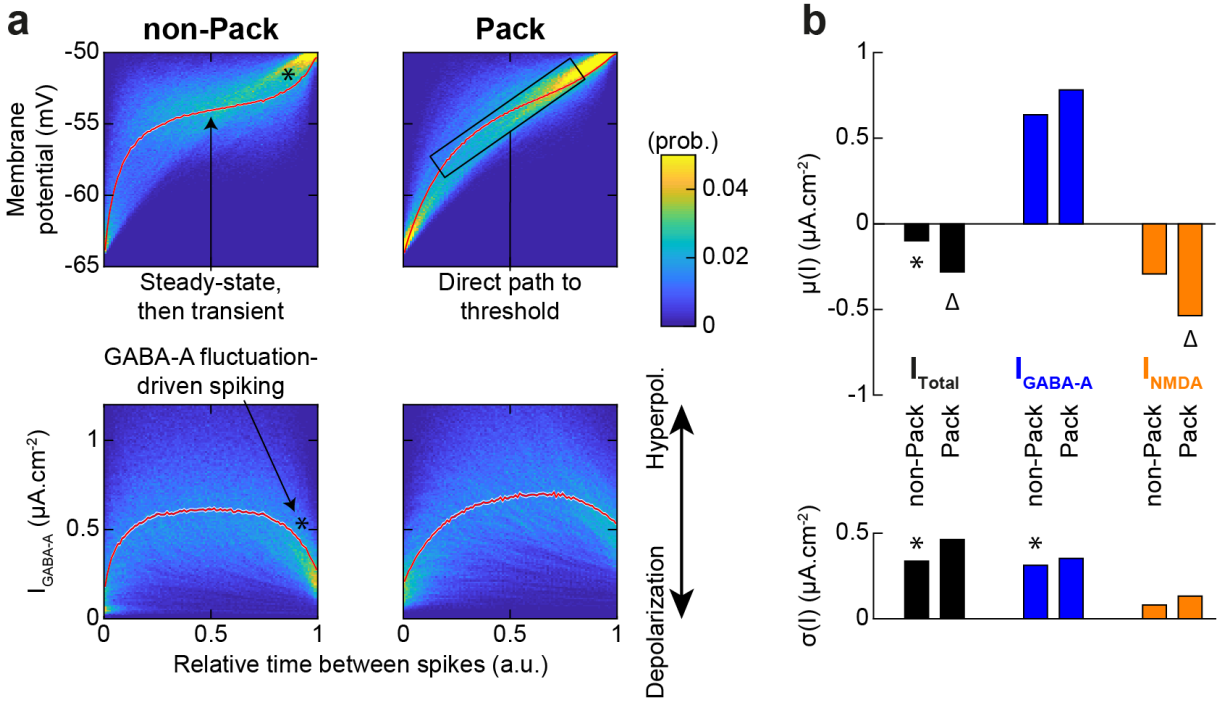

Figure 2. Pack propagation relies on a transition from GABA-A fluctuation- to NMDA mean current-driven deterministic spiking. (**a**) Membrane potential (top) and GABA-A current (bottom) of neurons when outside (left) and within (right) the trajectory activity pack, considered at the time scale of an ISI or between two spikes. Data is aggregated by normalizing time between two spikes (no matter the ISI duration). Background color shows the probability of individual membrane potentials or GABA-A currents curves (sum normalized to 1 in each time bin) across many ISI during one network simulation of 4 seconds, with red curves showing the average (weighted according to the underlying probabilities at each time bin). (**b**) Temporal average (top) and fluctuations (bottom) of total (left, black), GABA-A (middle, blue) and NMDA (right, orange) currents onto neurons when outside (non-Pack) or within (Pack) the trajectory activity pack, averaged across neurons.

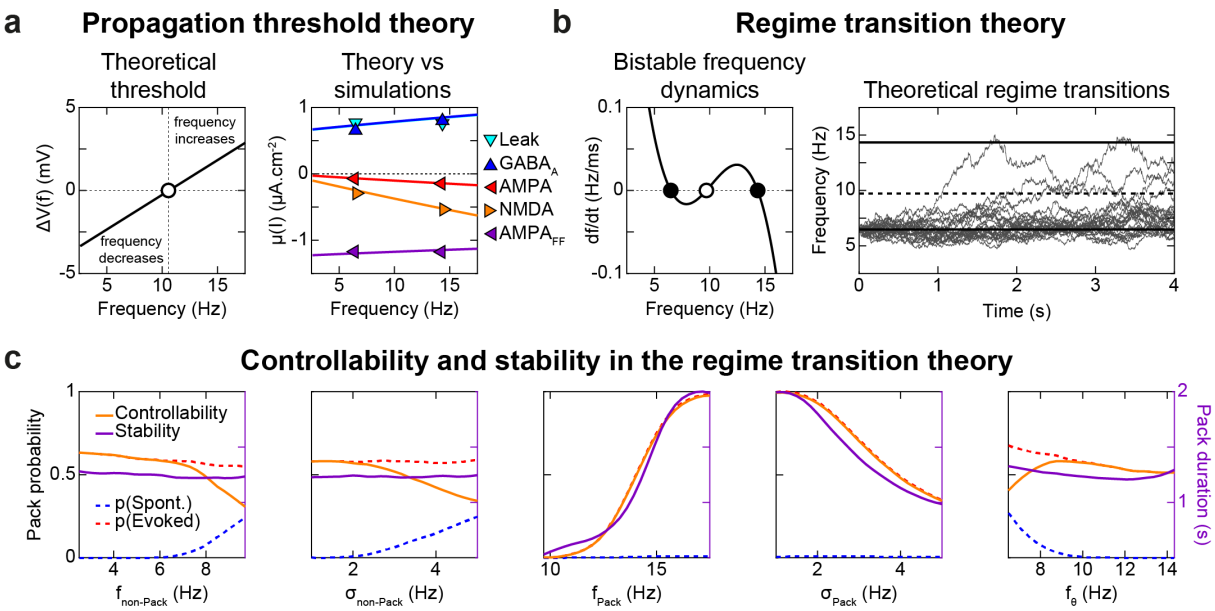

Figure 3. Theoretical account of the threshold separating, and transitions between, spontaneous and propagation regimes (**a**) Propagation threshold theory. (Left) In a 1D reduced analytical model (see Methods), frequency self-amplifies above f_θ and is extinguished below, i.e. as the membrane potential reaches ($\Delta V > 0$) or not ($\Delta V < 0$) a fluctuation-based spiking threshold at time $T = 1/f$ in a postsynaptic neuron, given presynaptic spiking at frequency f. (Right) The theoretical model is quantitatively consistent with network simulations at the fine-grain of ionic and synaptic currents in both the low frequency spontaneous and the higher frequency pack regimes. (**b**) Regime transition theory. (Left) In a 1D reduced model of both regimes, frequency dynamics follows bistable dynamics with added Gaussian noise. (Right) Example simulations of the regime transition theory. (**c**) Probability of spontaneous and evoked transitions to the regime of pack propagation (dotted lines), and of controllability and stability of the pack regime (solid lines) in the regime transition theory, as a function of parameters (non-Pack and Pack mean frequencies and standard deviations, and the threshold frequency).

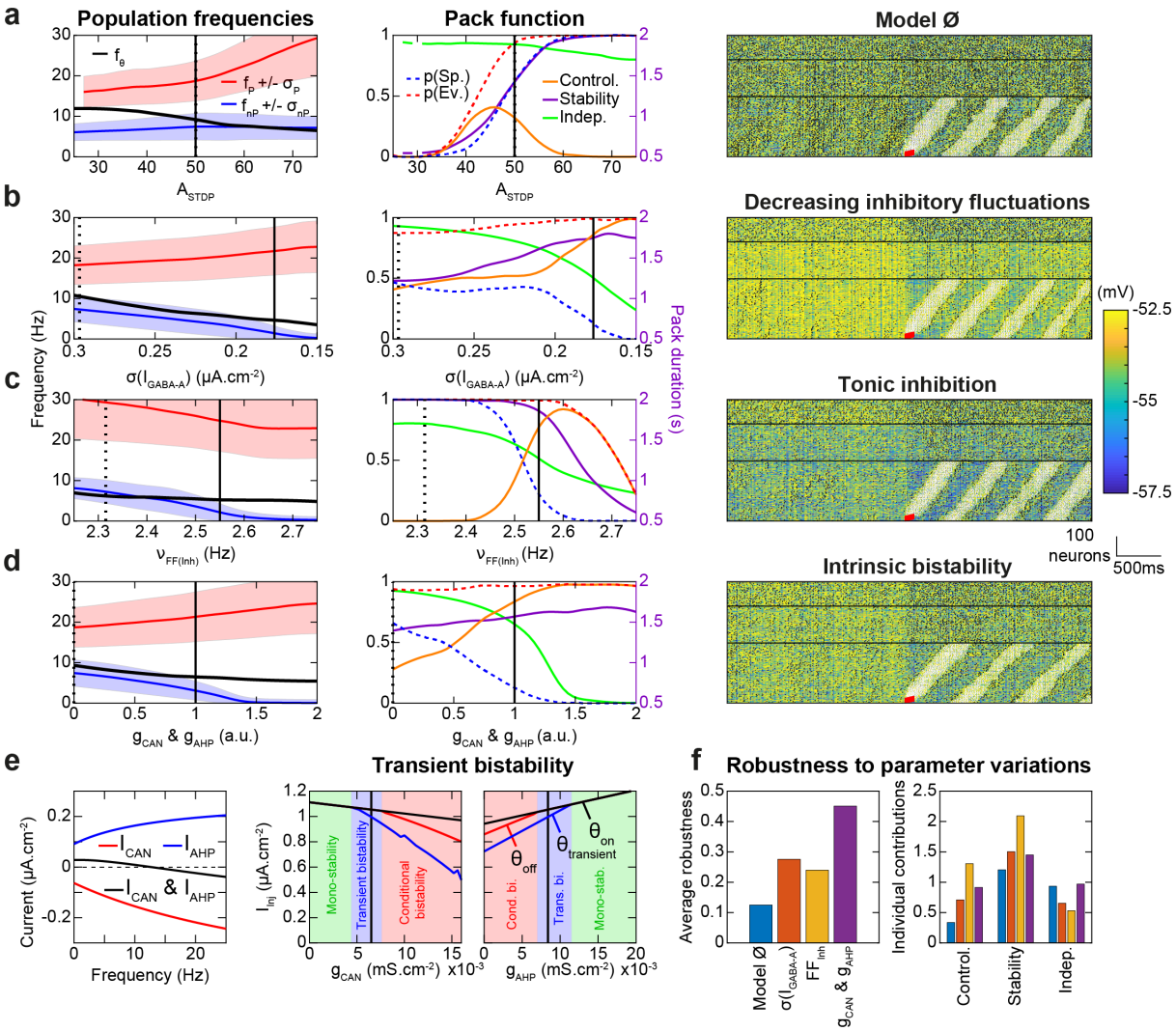

Figure 4. Modulation of controllability and stability by architectural, synaptic, and ionic determinants. (**a-d**) Mechanisms for increasing trajectory replay controllability and stability, as seen when varying different parameters, such as the GABA-A current fluctuations $\sigma(I_{GABA-A})$ (via a higher number of inh. → exc. synapses, see *Methods*) (**b**), the frequency of external neurons sending AMPA feedforward currents onto inhibitory neurons FF_{Inh} (**c**), and a multiplicative factor modulating CAN and AHP calcium-activated suprathreshold conductances together g_{CAN} & g_{AHP} (**d**). STDP amplitude A_{STDP} was varied across the different mechanisms (A_{STDP} = 47.5 for $\sigma(I_{GABA-A})$, 75 for FF_{Inh} and 50 for g_{CAN} & g_{AHP}), and is shown as a control for comparison's sake in (**a**). (Left) Non-pack and pack average frequency (+/- fluctuations) and threshold frequency, when varying the aforementioned parameters (X-axis). Normal parameter value (dotted vertical black line), and that chosen to illustrate the mechanism's effects (solid vertical black line), are indicated. (Middle) Probability of spontaneous and evoked packs (dotted lines), and pack controllability, propagation stability and independence (solid lines). (Right) Example of trajectory replay with illustrative mechanism parameters. The (A_{STDP}, mechanism parameter) value couple of each mechanism was systematically determined as that maximizing the product of controllability, stability and independence (all three being normalized

between 0 and 1). (**e**) (Left) Equilibrium values of CAN (red), AHP (blue) and total (CAN & AHP, black) currents of excitatory neurons, when considering the time-averaged calcium concentration at different frequencies. (Right) CAN and AHP calcium-activated suprathreshold conductances induced transient spiking bistability (rather than mono-stability, conditional bistability or absolute bistability), as defined by the protocol in [29] (see *Methods*). Solid vertical black lines indicate the chosen mechanism parameters. (**f**) (Left) Average robustness of the physiological low-frequency asynchronous irregular network activity with controllable, stable and independent trajectory replays, to the variation of 22 of the model's parameters (see *Methods* and **Fig. S3**). The different mechanisms, and the standard Model (∅), are compared. (Right) Contribution of the trajectory replay controllability, stability and independence criteria to the overall robustness score.

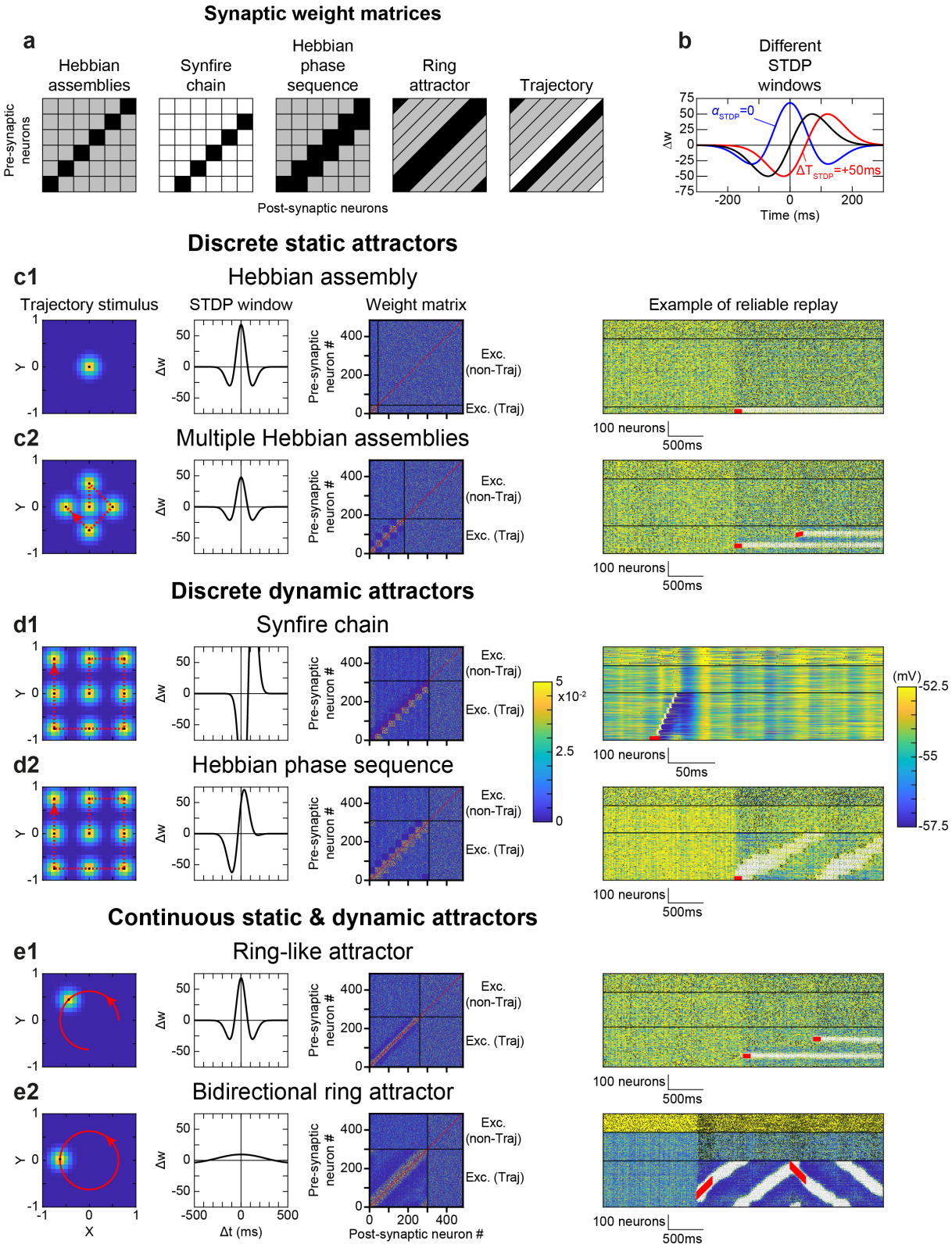

Figure 5. A common framework for attractor models. (**a**) Weight matrices underlying different types of network attractors. White, grey and black colors indicate the strength of synaptic weights (white = absence of synapses, grey = moderate weights, black = strong weights). (**b**) Modulation of the asymmetric STDP window (black) when varying its symmetry ($\alpha_{STDP} = 0$, symmetric STDP window, blue curve) and temporal shift ($\Delta t = +50ms$, red curve). (**c-e**) Altering the trajectory stimulus and

STDP learning rule, when combined with the aforementioned mechanisms allowing controllable and stable trajectory replays, enabled the emergence of reliable attractors of different types, e.g. discrete vs. continuous and static vs. dynamic attractors, as in (a). (Left) External trajectory stimulus (as in **Fig. 1.d** left). Dotted red lines indicate a discontinuous trajectory, jumping from one black dot to the next in a discrete manner (rather than continuously, as in (e)). (Middle left) STDP temporal window (as in **Fig. 1.d** middle). (Middle right) Resulting synaptic weight matrices between presynaptic and postsynaptic excitatory neurons on the Y- and X-axes respectively. Neurons affected by the trajectory are regrouped and ordered according to their activation time within the learned trajectory stimulus. (Right) Examples of resulting trajectory replay. The g_{CAN} & g_{AHP} mechanism was used for the Hebbian assembly, multiple Hebbian assemblies and ring-like attractors; the $\sigma(I_{GABA-A})$ mechanism was used for the synfire chain, Hebbian phase sequence and bidirectional ring attractors; the $\nu_{FF(Inh)}$ mechanism was used for the synfire chain. Additional modifications were necessary for the synfire chain ($g_{AMPA} = 0.5\ mS.cm^{-2}$, $g_{NMDA} = 0\ mS.cm^{-2}$ instead of $0.2\ mS.cm^{-2}$, $g_{NMDA} = 0.3\ mS.cm^{-2}$ for rapid pack propagation) and bidirectional ring attractors (see *Methods*).

Supplementary Figures

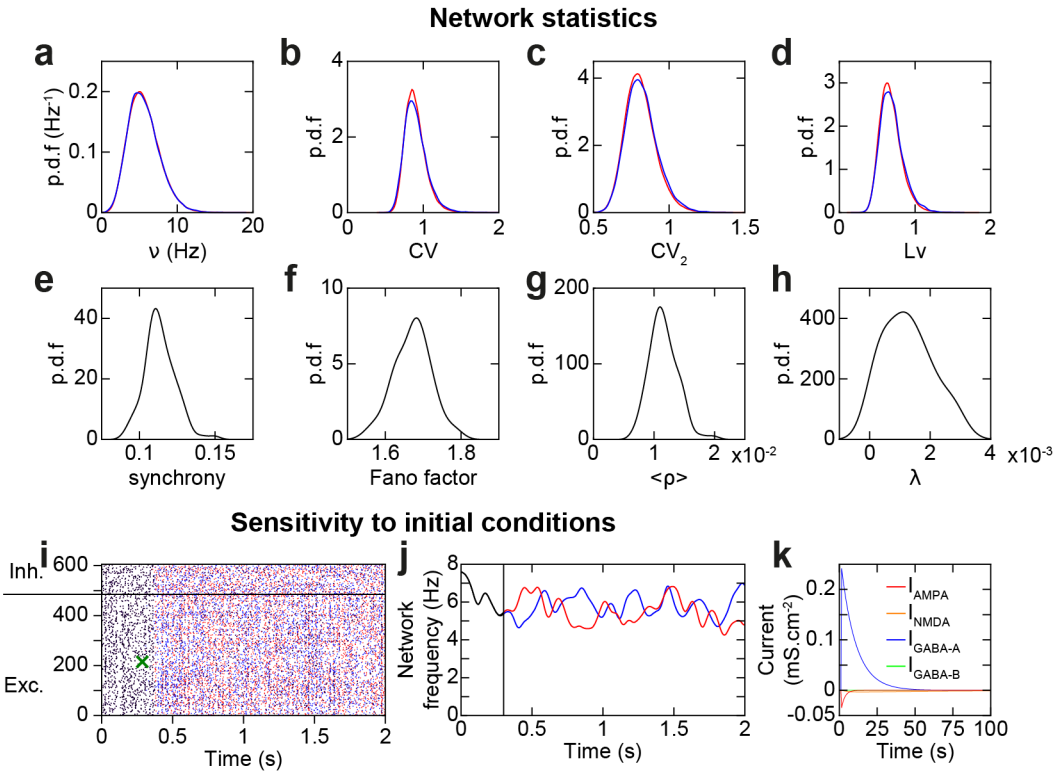

Figure S1. Distributions of network statistics over many network simulations. (**a-h**) Probability density functions of network spiking statistics, calculated on 100 network simulations of 10s. Frequency (**a**), CV (**b**), CV2 (**c**), and Lv (**d**) of individual excitatory (red) and inhibitory (blue) neuronal spiking activity. Synchrony measure (**e**), Fano factor (**f**), average pairwise correlation coefficient (**g**), and Lyapunov exponent (**h**) of network spiking activity. (**i**) Chaotic network activity seen through sensitivity to initial conditions. A network was simulated in identical initial conditions, until a single randomly chosen spike at ~300ms (green cross) was either kept (red spikes) or removed (blue spikes). Overlap in spikes between in both simulations are colored in black (notice that all spikes are identical and thus black before the green cross). (**j**) Same as (i), but average network frequency of both simulations (red & blue, overlap in black). (**k**) Stronger IPSC than EPSC, allowing balanced total currents and thus fluctuation-based spiking. IPSC and EPSC are subdivided into their individual (AMPA, NMDA, GABA-A, GABA-B) components.

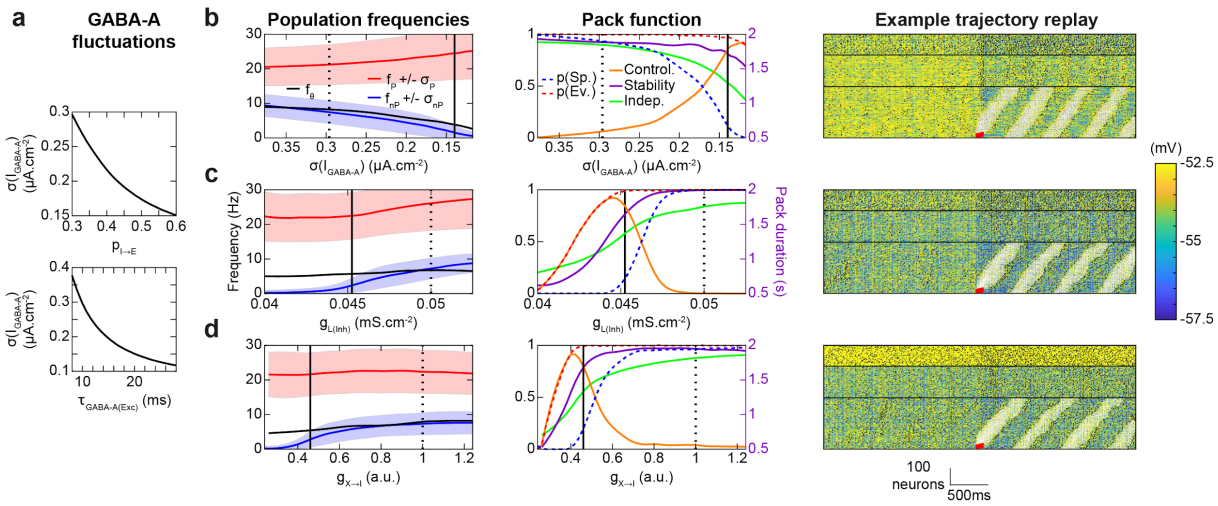

Figure S2. GABA-A fluctuations and alternative effects of lowering disinhibition on replay quality. (**a**) $\sigma(I_{GABA-A})$ as a function of $f_{I\to E}$ or $\tau_{GABA-A(Exc)}$. (**b-d**) Same as **Fig. 4a-d**, but when varying the GABA-A current time constant of excitatory neurons $\tau_{GABA-A(Exc)}$ ($A_{STDP} = 57.5$) (**b**), leak conductance of inhibitory neurons $g_{L,(Inh)}$ ($A_{STDP} = 67.5$) (**c**), and multiplicative factor of recurrent current conductances impinging upon inhibitory neurons $\rho_{X\to I}$ ($A_{STDP} = 60$) (**d**). For $\tau_{GABA-A(Exc)}$, Δp of inhibitory to excitatory neuron synapses were modulated in order for average p_{GABA-A} to be kept approximately constant at $\nu = 5.5\ Hz$, i.e. weakened for longer $\tau_{GABA-A(Exc)}$. To do so, Δp was multiplied by the estimated average p_{GABA-A} value at $\nu = 5.5\ Hz$ for the standard value of $\tau_{GABA-A(Exc)} = 10\ ms$ (calculated as for $p_{AMPA_{FF}}$) and divided by the same estimate but for the chosen value of $\tau_{GABA-A(Exc)}$.

Robustness to each individual parameter

a

Categories	Parameters
Synaptic matrix	μ_w, σ_w, A_{STDP}, τ_{STDP}, α_{STDP}
Recurrent synaptic currents	g_{AMPA}, g_{NMDA}, g_{GABA-A}, g_{GABA-B}, τ^{Decay}_{AMPA}, τ^{Decay}_{NMDA}, τ^{Decay}_{GABA-A}, τ^{Decay}_{GABA-B}, k_{NMDA}, α_{NMDA}, τ^{Rise}_{NMDA}, α_{GABA-B}, τ^{Rise}_{GABA-B}
Stimulus & intrinsic properties	σ_{RF}, υ_{Traj}, g_{Leak}, $g_{AMPA.FF}$

b

Criteria	Accepted range	References
Physiological peak IPSC/EPSC ratio	$5 \leq x \leq 10$	(Xue et al., 2014)
Physiological peak NMDA/AMPA ratio	$1 \leq x \leq 2$	(Myme et al., 2003; Wang et al., 2008)
Sustained network activity	$x \leq 100$ms	
Physiological neuronal activity	$x \leq 250$ms	
Physiological Exc. frequency	$0.1 \leq x \leq 15$Hz	(Boudewijns et al., 2013; Shafi et al., 2007)
Physiological Inh. frequency	$0.1 \leq x \leq 30$Hz	(Boudewijns et al., 2013; Shafi et al., 2007)
Physiological Exc. spontaneous CV	$0.5 \leq x \leq 1.5$	(Compte et al., 2003)
Physiological Exc. spontaneous CV2	$0.25 \leq x \leq 1.25$	(Compte et al., 2003)
Low pack frequency	$15 \leq x \leq 100$Hz	(Xue et al., 2014)
Controllability	$x = 1$	(Harvey et al., 2012; Jadhav et al., 2016)
Stability	$x \geq 1$s	(Harvey et al., 2012; Jadhav et al., 2016)
Independence	$0.5 \leq x \leq 1$	(Harvey et al., 2012)

c

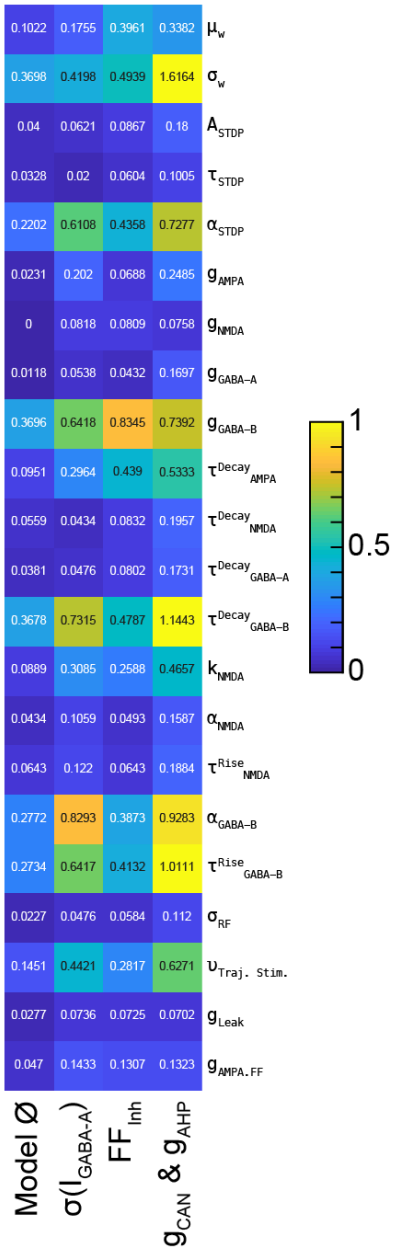

Figure S3. Robustness to parameters. Computation of the robustness score, quantifying to what extent the physiological low-frequency asynchronous irregular network activity with controllable, stable and independent trajectory replays is robust to the variation of the model's parameters. (**a**) Parameters varied (see *Methods*). (**b**) List of criteria that need to be simultaneously met within a model network simulation for it to be considered "correct". (**c**) Detail of the robustness score for each individual model parameter, for the different mechanisms and standard model (Ø).

Methods

Model of biophysical local recurrent neural network

We built a biophysical model of a generic local recurrent neural network, endowed with detailed biological properties of its neurons and connections, as in [28]. The network model contained N neurons that were either excitatory (E) or inhibitory (I) (neurons projecting only glutamate or GABA, respectively, [51]), with probabilities p_E and $p_I = 1 - p_E$ respectively, and $\frac{p_E}{p_I} = 4$ [52]. Connectivity was sparse (i.e. only a fraction of all possible connections exists, see $p_{E\to E}, p_{E\to I}, p_{I\to E}, p_{I\to I}$ parameter values, [53]) with no autapses (self-connections) and EE connections (from E to E neurons) drawn to ensure the over-representation of bidirectional connections in cortical networks (four times more than randomly drawn according to a Bernoulli scheme, [54]). The synaptic weights $w_{(i,j)}$ of existing connections were drawn identically and independently from a log-normal distribution of parameters μ_w and σ_w [54]. To cope with simulation times required for the massive explorations ran in the parameter space, neurons were modeled as leaky integrate-and-fire (LIF) neurons.

The membrane potential followed

$$\begin{cases} C\dfrac{dV_{(j)}}{dt} = -(I_{Ionic(j)} + I_{Syn.Rec(j)} + I_{Syn.FF(j)}) \\ V_{(j)} > \theta \to V_{(j)} = V_{rest} \end{cases}$$

where neurons spike when the membrane potential reached the threshold θ, and repolarization to V_{rest} occurred after a refractory period Δt_{AP}. Initial membrane potential of neurons were randomly drawn from a uniform distribution between θ and V_{rest}.

The ionic current followed

$$I_{Ionic(j)} = I_{L(j)} + I_{CAN(j)} + I_{AHP(j)}$$

in which the leak current was

$$I_L = \bar{g}_L \left(V_{(j)} - V_L\right)$$

where $\bar{g}_L$ was the maximal conductance and V_L the equilibrium potential of the leak current.

The cationic non-selective (I_{CAN}) current and the medium after-hyperpolarization (I_{AHP}) currents, responsible for frequency adaptation and bistable discharge in pyramidal neurons, were taken as

$$I_x = \bar{g}_x \, p_x^{\gamma_x} \left(V_{(j)} - V_x \right)$$

where p_x ($x \in \{CAN, AHP\}$) corresponded to the opening probability of both currents and γ_x the gating factor of opening probabilities. Denoting the intra-somatic calcium concentration as Ca, p_x followed

$$\frac{dp_x}{dt} = \frac{(p_x^{\infty}(Ca) - p_x)}{\tau_x(Ca)}$$

with

$$\tau_x(Ca) = \frac{1}{(\alpha_x Ca + \beta_x)}$$

and

$$p_x^{\infty}(Ca) = \frac{\alpha_x Ca}{(\alpha_x Ca + \beta_x)}$$

where α_x and β_x respectively denoted activation and deactivation kinetic constants, consistent with experimental data in layer 5 PFC pyramidal neurons [55–57].

The intra-somatic calcium concentration evolved according to discrete spike-induced increments and first-order exponential decay

$$\frac{dCa_{(j)}}{dt} = \frac{Ca_0 - Ca_{(j)}}{\tau_{Ca}} + \Delta Ca\ \delta\left(t - t_{(j)}^{k}\right)$$

where $t_{(j)}^{k}$ was the time of the k_{th} spike in the spike train of neuron j, δ the Dirac delta function, τ_{Ca} the time constant of calcium extrusion, Ca_0 the basal calcium and ΔCa a spike-induced increment of calcium concentration.

The recurrent synaptic current on postsynaptic neuron j, from – either excitatory or inhibitory – presynaptic neurons (indexed by i), was

$$I_{Syn.Rec(j)} = \sum_{i} \left(I_{AMPA(i,j)} + I_{NMDA(i,j)} + I_{GABA_A(i,j)} + I_{GABA_B(i,j)}\right)$$

The delay for synaptic conduction and transmission, Δt_{syn}, was considered uniform across the network [58]. Synaptic recurrent currents followed

$$I_{x(i,j)} = \bar{g}_x\ w_{(i,j)}\ p_{x(i)}\left(V_{(j)} - V_x\right)$$

with $w_{(i,j)}$ the synaptic weight. The NMDA current followed

$$I_{NMDA(i,j)} = \bar{g}_{NMDA}\ w_{(i,j)}\ p_{NMDA(i)}\ x_{NMDA}\left(V_{(j)}\right)\left(V_{(j)} - V_{NMDA}\right)$$

incorporating the magnesium block voltage-dependence modeled [59] as

$$x_{NMDA}(V) = \frac{1}{\left(1 + [Mg^{2+}]\frac{e^{-0.062\,V}}{3.57}\right)}$$

AMPA and $GABA_A$ rise times were approximated as instantaneous [58] and bounded, with first-order decay

$$\frac{dp_{x(i)}}{dt} = -\frac{p_{x(i)}}{\tau_x^{decay}} + \Delta p_x\ \left(1 - p_{x(i)}\right)\ \delta\left(t - t_{(i)}^{k}\right)$$

To take into account the longer NMDA [60] and GABA-B [61] rise times, opening probabilities followed second-order dynamics [58]

$$\begin{cases} \dfrac{dq_{x(i)}}{dt} = -\dfrac{q_{x(i)}}{\tau_x^{rise}} + \Delta q_x \left(1 - q_{x(i)}\right) \delta\left(t - t_{(i)}^k\right) \\ \dfrac{dp_{x(i)}}{dt} = -\dfrac{p_{x(i)}}{\tau_x^{decay}} + \alpha_x \, q_{x(i)} \left(1 - p_{x(i)}\right) \end{cases}$$

Recurrent excitatory and inhibitory currents were balanced in each postsynaptic neuron [24], according to driving forces and the excitation/inhibition weight ratio, through

$$\begin{cases} \bar{g}_{GABA_A} = g_{GABA_A} \dfrac{-(V_{mean} - V_{Exc})}{\left(V_{mean} - V_{GABA_A}\right)} \dfrac{\sum_{i \in Exc} w_{(i,j)}}{\sum_{i \in Inh} w_{(i,j)}} \\ \bar{g}_{GABA_B} = g_{GABA_B} \dfrac{-(V_{mean} - V_{Exc})}{\left(V_{mean} - V_{GABA_B}\right)} \dfrac{\sum_{i \in Exc} w_{(i,j)}}{\sum_{i \in Inh} w_{(i,j)}} \end{cases}$$

with $V_{mean} = \frac{(\theta + V_{rest})}{2}$ being an approximation of the average membrane potential. The excitation/inhibition weight ratio notably balanced the currents coming from inhibitory neurons with the 4x more numerous excitatory neurons (rendering inhibitory currents 4x stronger on average). When specified (**Fig. S2.d**), both excitatory and inhibitory conductances onto excitatory neurons were multiplied by $g_{X \to E}$, and onto inhibitory neurons by $g_{X \to I}$.

The feed-forward synaptic current $I_{Syn.FF(j)}$ (putatively arising from sub-cortical and cortical inputs) consisted of an AMPA component

$$I_{Syn.FF(j)} = \bar{g}_{AMPA} \, p_{AMPA_{FF}} \left(V_{(j)} - V_{AMPA}\right)$$

with a constant opening probability $p_{AMPA_{FF}}$, determined as the temporal average of AMPA channel openings due to n_{FF} neurons within putatively sub-cortical and cortico-cortical structures spiking at a given frequency ν_{FF}, following

$$p_{AMPA_{FF}} = \tau_{AMPA}\, n_{FF}\, \nu_{FF} \frac{\Delta p_{AMPA}\left(1 - e^{-\frac{1}{\tau_{AMPA}\, n_{FF}\, \nu_{FF}}}\right)}{1 + (\Delta p_{AMPA} - 1)\, e^{-\frac{1}{\tau_{AMPA}\, n_{FF}\, \nu_{FF}}}}$$

via integration (considering regular ISI for simplification during the integration). $p_{AMPA_{FF}}$ was considered constant so as to isolate the influence of deterministic chaos and spike irregularity on trajectory replay. However, to guarantee an initial stimulation sufficiently strong to start network activity, feedforward AMPA inputs were stronger at first ($n_{FF} = 200$ neurons, $\nu_{FF} = 3\ Hz$) and progressively decreased during $250\ ms$ to their final value ($\nu_{FF} = 2.315\ Hz$; these initial $250\ ms$ were cut from all figures and analyses). Trajectory replay was evoked 2s after the initial 250ms (**Fig. 1e-h**, red square) when the first 25 neurons of the trajectory received a strong feedforward AMPA stimulation ($n_{FF} = 20$ neurons, $\nu_{FF} = \nu_{Traj.Stim.} = 50\ Hz$, emulating a strong signal coming from few neurons). The epoch before this trajectory-evoking stimulus was considered "Spontaneous" and the epoch after "Evoked".

Learning protocol

The neural network was subjected to "offline" learning, i.e. before the network simulation, during which the receptive fields of excitatory neurons were sequentially stimulated. The resulting neural frequency conditioned learning of synaptic weights via STDP between excitatory neurons. This "offline" learning procedure would correspond to the trajectory stimulus being learned and memorized long before the network simulation.

Neuronal receptor fields existed in a 2D spatial area (**Fig. 1d** left) following non-normalized bivariate Gaussian functions around their center points (x_j, y_j) organized along a square grid. For a stimulation point $s\ (x_s(t_s), y_s(t_s))$ of intensity I_s at moment t_s, the resulting neural frequency of the stimulation of the receptive field was

$$\nu_j(t_s) = I_s\, e^{-\left(\frac{(x_j - x_s(t_s))^2 + (y_j - y_s(t_s))^2}{\sigma_{RF}^2}\right)}$$

This stimulation was part of a dynamic spatiotemporal trajectory moving as time went by. The synaptic weights between neurons were then altered in proportion to their frequencies

according to a phenomenological STDP rule (see below). A circular trajectory was chosen in order to study the sequence replay stability across multiple circle loops. The trajectory stimulus advanced by 0.05 (in the spatial area reference) every $dt_{Traj} = 20\ ms$ time step, with a small overlap between the trajectory start and end to ensure looping. For discrete stimuli (**Fig. 5**), the trajectory cycled 10x through the shown sequence of black dots (with the same trajectory time step). Neurons were considered as belonging to the trajectory when any of their stimulation-induced $\nu_j(t_s) > 5\%$ of the maximum neuron frequency the trajectory produced.

Spike-timing dependent plasticity

We assessed various STDP temporal windows, from entirely asymmetric ($\alpha_{STDP} = 1$) to symmetric ($\alpha_{STDP} = 0$) and time-shifted (ΔT_{STDP}) functions. To modulate STDP symmetry, we identified two STDP functions, an asymmetric and a symmetric one (whose integrals equal 0, so that LTP and LTD contributions are balanced), and then performed a linear combination of both to obtain various degrees of STDP temporal asymmetry. However, even though the integral stayed null, the integral of the positive part changed, which we corrected by normalizing according to the asymmetric function's integral's positive part. As such, the STDP function followed

$$f_{asym}(\Delta t) = A_{STDP}\sqrt{2e}\,\frac{\Delta t - \Delta T_{STDP}}{\tau_{STDP}}\,e^{-\left(\frac{\Delta t - \Delta T_{STDP}}{\tau_{STDP}}\right)^2}$$

$$f_{sym}(\Delta t) = A_{STDP}\left(1 - 2\left(\frac{\Delta t - \Delta T_{STDP}}{\tau_{STDP}}\right)^2\right)e^{-\left(\frac{\Delta t - \Delta T_{STDP}}{\tau_{STDP}}\right)^2}$$

$$f_{mixed}(\Delta t) = \alpha_{STDP} f_{asym}(\Delta t) + (1 - \alpha_{STDP}) f_{sym}(\Delta t)$$

$$f_{STDP}(\Delta t) = f_{mixed}(\Delta t)\,\frac{\int_{f_{asym}(\Delta t)>0} f_{asym}(\Delta t)}{\int_{f_{mixed}(\Delta t)>0} f_{mixed}(\Delta t)}$$

where $\Delta t = t_{post} - t_{pre}$ was the temporal difference between pre- and postsynaptic spikes, A_{STDP} the STDP amplitude and τ_{STDP} the STDP time constant. As such, taking into account the frequencies of pre- and postsynaptic neurons and the time difference between stimulation times, the weights were changed according to

$$\Delta w_{ij}(t_{s_1}, t_{s_2}) = \sum_{t_{s_1}} \sum_{t_{s_2}} \nu_i(t_{s_1}) \nu_j(t_{s_2}) f_{STDP}(\Delta t)$$

with $\Delta t = t_{s_2} - t_{s_1}$. A lower hardbound limit ($w \geq 0$) was imposed after STDP learning, whereas no upper hardbound limit was imposed.

Synaptic scaling

In order to keep neuronal activity within certain putative homeostatic bounds [26], synaptic weights entering a postsynaptic neuron are subjected after STDP learning to a simple multiplicative phenomenological form of synaptic scaling, potentially representing hetero-synaptic LTD, where the sum of weights impinging upon a pyramidal neuron is kept constant before and after STDP. This is written

$$w_{Scaled(i,j)} = w_{After\ STDP(i,j)} \frac{\sum_i \ w_{Before\ STDP(i,j)}}{\sum_i \ w_{After\ STDP(i,j)}}$$

Detection of packs

In order to detect propagating activity pulse packets along the synaptic pathway, we first convolved neural spiking activity with a centered normalized Gaussian function where $\sigma = 30ms$, to then spatially convolute it with the bivariate Gaussian receptive field function (see above) centered on the discrete points of the spatiotemporal trajectory. Such smoothing procedures allowed us to reliably choose a frequency threshold ($12.5Hz$) above which trajectory point were considered "active". Conversely, from these "active" trajectory points, we considered trajectory neurons "active" when at least 40% of the trajectory points having stimulated that neuron's receptive field (above the aforementioned 5% of maximum neuron frequency), weighted by the neural frequency resulting from trajectory stimulation, were "active". This allowed us to define pack emergence as when at least 20 dynamically changing trajectory neurons were "active" on average during 500 successive milliseconds (ensuring activity packets were strong enough, e.g. **Fig. 1e-h** white spikes).

Determining pack and non-pack frequency average, fluctuations or threshold

f_{nP} and σ_{nP} were determined as the frequency average and fluctuations of the aforementioned spatially-convoluted trajectory points of neurons outside the pack during periods without packs, while f_P and σ_P were similarly determined but for neurons within the pack during packs. By manipulating the frequency of neurons within the trajectory f_T through different levels of feedforward AMPA currents, the frequency threshold f_θ was determined as the minimal f_{nP} for which packs propagate constantly ($\geq 1900\ ms$ out of $2\ s$ total, and $p_{Spont} \geq 0.95$). This understanding derived from the predictions of the bistable and noisy regime transition model, mimicking the process where the non-pack frequency f_{nP} stable fixed point increases until it annihilates with the threshold f_θ unstable fixed point (as in a saddle-node bifurcation), in which case only the pack frequency f_P stable fixed point remains and packs thus propagate constantly.

Maximum Lyapunov Estimate

To quantify the chaotic nature of the network's activity, we estimated the maximum Lyapunov exponent λ on the one-dimensional time series of the estimated instantaneous spiking frequency ($\sigma = 30\ ms$) averaged across excitatory neurons, based on the MATLAB program developed by Wolf and colleagues [62]. To do so, we reconstructed the phase space through time-delay embedding with heuristics agreed upon in the literature [63,64]. The lag length was estimated as the first lag length for which the autocorrelation coefficient $AC < e^1$ [65]. The embedding dimension was estimated via a MATLAB program developed by "Mirwais" Kizilkaya [66] according to the false nearest neighbor method [66,67] as the minimal dimension with 0% false nearest neighbors as determined by tolerance factors ($R_{tol} = 10$, $A_{tol} = 2$, [66]).

Spiking variability and synchrony

Spiking variability and synchrony measures are calculated as in [28]. In an effort to compare spike variability between our model and experimental data, we quantified the coefficient of variation (CV) of the inter-spike interval (ISI) distribution of the spiking trains of neurons in the network [19] according to

$$CV = \frac{\sigma_{ISI}}{\mu_{ISI}}$$

However, the CV measure assumes stationarity of the data. Since this assumption isn't necessarily verified, we also computed the CV2 and Lv of the spike trains to evaluate the variability of ISIs at a local level, according to

$$CV_2 =< 2\frac{|ISI_{k+1} - ISI_k|}{ISI_{k+1} + ISI_k} >_k$$

$$Lv =< 3\frac{(ISI_k - ISI_{k+1})^2}{(ISI_k + ISI_{k+1})^2} >_k$$

$CV = CV_2 = Lv = 1$ for an ISI distribution drawn from homogeneous Poisson spike trains and $= 0$ for perfectly regular spike trains (all ISI are equal). CV typically stand around 1 to 1.5 *in vivo*, while CV2 and Lv stand around 0.25 to 1.25 and 0 to 2 respectively *in vivo* [19,68]. CV was calculated on all ISI, while CV2 and Lv are calculated for each neuron then averaged across neurons.

Multiple synchrony measures were calculated, a synchrony measure S [69], pairwise correlation coefficient averaged over all pairs of neurons $< \rho >$ [20], and Fano factor F, following

$$S = \sqrt{\frac{Var(< f >_n)}{< Var(f_{(n)}) >_n}}$$

$$< \rho >= \frac{1}{N(N-1)/2}\sum_i \sum_{j>i} \frac{cov(f_{(i)}, f_{(j)})}{\sqrt{Var(f_{(i)})Var(f_{(j)})}}$$

$$F = \frac{Var(\sum_n s_n)}{< \sum_n s_n >_t}$$

where f was the estimated instantaneous neural spiking frequency via Gaussian convolution ($\sigma = 30ms$), n the neuron index, and s the population sum of spike counts, where $S = \frac{1}{\sqrt{N}} \sim 0.041$, $< \rho >= 0$ and $F = 1$ for perfectly asynchronous network activity, and $S =< \rho > = 1$ while F increases for perfectly synchronous network activity.

Protocol for assessing the nature of intrinsic bistability

The protocol for evaluating the nature of neural intrinsic bistability, taken from [29], consisted of a strong phasic input (of amplitude $2\theta_{on}$ during $200\ ms$) followed by a weaker delay-period tonic input (of amplitude I_{Inj} during $10s$), in order to reveal conditional bistability activated by the phasic input but conditional on (i.e. requiring the) weaker delay-period tonic input. θ_{on} corresponded to the minimal delay-period tonic input current required to induce sustained firing during the delay without the strong initial phasic input, and θ_{off} the same but with the strong initial phasic input. $\theta_{transient}$ was the same as θ_{off} but corresponded to the minimal delay-period tonic input required to induce unstable (rather than sustained) firing. Firing was considered sustained when there were three or more spikes during the last $2\ s$ of the tonic input with stable ISIs (determined when $< \frac{ISI_{k+1}-ISI_k}{ISI_k} >_k$ was inferior to 0.05). Otherwise, firing was considered unstable for a single spike beyond 25ms after the initial phasic input, or for two spikes or more during non-sustained firing.

When $\theta_{on} = \theta_{off} = \theta_{transient}$, the neuron was considered monostable, i.e. the strong initial input current did not activate any intrinsic mechanisms generating sustained firing. When $\theta_{on} = \theta_{off} > \theta_{transient}$, the neuron was considered transiently bistable, the strong initial input inducing weak mechanisms generating unstable (but not sustained) firing. When $\theta_{on} > \theta_{off}$, the neuron was considered conditionally bistable, since the delay-period input, weaker than the initial phasic input but non-zero, could induce sustained firing, bistability being thus conditional upon the delay-period input. Finally, if $\theta_{on} > 0 > \theta_{off}$, the neuron's bistability was considered absolute, i.e. sustained neuronal firing after an initial input lasts until a hyperpolarizing current stops it.

Calculating robustness to variability of the model's parameters

We studied how sensitive the phenomenon of interest (namely controlled, stable and independent trajectory replay with asynchronous irregular network dynamics) was to the variability of model parameters, since biological systems present strong variability. To do so, we systematically varied important parameters, and defined a list of criteria which all need to be met (**Fig. S3**), encompassing physiological peak conductance ratios (top row), spiking activity regime (middle row) and controllable stable independent trajectory replays (bottom row). Sustained network activity (middle row) was determined when the maximal duration

without network spikes was 100ms, to exclude strongly oscillating networks prohibiting controllable trajectory replay. Physiological neuronal activity was determined when neuronal activity was 100Hz at most for 250ms (in order to exclude trivial trajectory replay cases where replay was actually detected as a single neuron stably firing at 100Hz during 500ms). CV and CV2 were determined during the spontaneous epoch (before the trajectory replay evoking stimulus at 2s, **Fig. 1e-h**).

Parameters were varied over a range of 40 equally-spaced values, generally spanning $\left(\frac{1}{3}, 3\right)$x the standard parameter value. Network simulations were repeated 5 times for each value (due to the potential variability of trajectory replays), with each repetition being evaluated independently concerning the criteria. The robustness score was calculated as

$$R = \frac{\Delta p}{< p >}$$

where $< p >$ represented the average correct parameter value (weighted by the proportion of correct repetitions), and Δp the sum of correct parameter steps (once again weighted by the proportion of correct repetitions), where a step was the difference between the next and previous parameter value divided by 2, or $\frac{|p_{k+1} - p_{k-1}|}{2}$ (values being equally spaced).

This robustness score was conservative no matter the arbitrarily chosen range, since it is a biased underestimation which approaches its true maximal limit value given an optimal chosen range. Indeed, robustness was limited by 1) how large the parameter range considered was, and 2) how close parameter steps were. The robustness score decreased from its true maximal value with ranges which were too small and step values too large. Contributions of individual criteria (**Fig. 4f**, right) were calculated as the Δp when considering only that one criteria (with the same $< p >$ value still calculated over all criteria, for better comparison of individual contributions).

Numerical integration and parameters of the biophysical network model

Models were simulated and explored using custom developed code under MATLAB and were numerically integrated using the forward Euler method with time-step $\Delta t = 0.5ms$ in network models.

Unless indicated in figure legends, standard parameter values were as following. Concerning the network architecture, $N = n_{Exc} + n_{Inh} = 605$ neurons, $p_{Exc} = 0.8$, so that $n_{Exc} = Np_{Exc} = 484$ neurons and $n_{Inh} = Np_{Inh} = 121$ neurons. Concerning Integrate-and-Fire neuron properties, $C = 1\ \mu F.cm^{-2}$, $V_{rest} = -65\ mV$, $\theta = -50\ mV$, $V_{mean} = \frac{V_{rest}+\theta}{2} = -57.5\ mV$, $\Delta t_{AP} = 3\ ms$. Concerning ionic currents, $\bar{g}_L = 0.05\ mS.cm^{-2}$, $V_L = -70\ mV$, $\bar{g}_{CAN} = 0\ mS.cm^{-2}$, $V_{CAN} = 30\ mV$, $\alpha_{CAN} = 0.03125\ \mu M^{-1}.ms^{-1}$, $\beta_{CAN} = 0.025\ ms^{-1}$, $\gamma_{CAN} = 1$, $\bar{g}_{AHP} = 0\ mS.cm^{-2}$, $V_{AHP} = -90\ mV$, $\alpha_{AHP} = 0.125\ \mu M^{-1}.ms^{-1}$, $\beta_{AHP} = 0.025\ ms^{-1}$, $\gamma_{AHP} = 1$, $\Delta Ca = 0.2\ \mu M$, $Ca_0 = 0.1\ \mu M$, $\tau_{Ca} = 100\ ms$. Concerning the weight matrix, $\mu_w = 0.03$, $\sigma_w = 0.015$, $p_{E\to E} = p_{E\to I} = p_{I\to I} = p_{I\to E} = 0.3$. Concerning synaptic currents, $\Delta t_{syn} = 0.5\ ms$, $\bar{g}_{AMPA} = 0.2\ mS.cm^{-2}$, $\tau_{AMPA}^{decay} = 2.5\ ms$, $\bar{g}_{NMDA} = 0.3\ mS.cm^{-2}$, $\alpha_{NMDA} = 0.275\ ms^{-1}$, $\tau_{NMDA}^{rise} = 4.65\ ms$, $\tau_{NMDA}^{decay} = 75\ ms$, $[Mg^{2+}] = 1.5\ mM$, $V_{AMPA} = V_{NMDA} = 0\ mV$, $g_{GABA_A} = 0.35\ mS.cm^{-2}$, $\tau_{GABA_A}^{decay} = 10\ ms$, $V_{GABA_A} = -70\ mV$, $g_{GABA_B} = 5.10^{-4}\ mS.cm^{-2}$, $\alpha_{GABA_B} = 0.015\ ms^{-1}$, $\tau_{GABA_B}^{rise} = 90\ ms$, $\tau_{GABA_B}^{decay} = 160\ ms$, $V_{GABA_B} = -90\ mV$, $\Delta p_{AMPA} = \Delta q_{NMDA} = \Delta p_{GABA_A} = \Delta q_{GABA_B} = 0.1$. Concerning the learning procedure and STDP, $\sigma_{RF} = 0.13$, $I_s = 0.02925$, $\tau_{STDP} = 100\ ms$, $A_{STDP} = 50$, $\alpha_{STDP} = 1$, $\Delta T_{STDP} = 0\ ms$.

Parameters for the biophysical mechanisms (**Fig. 4**) were systematically determined as the (A_{STDP}, mechanism parameter) value couple maximizing the product of controllability, stability and independence (all three being normalized between 0 and 1).

For the bidirectional ring attractor (**Fig. 5.e2**), model parameters were as followed: $p_{I\to E} = 0.4$, $g_{X\to E} = 1.5$, $g_{X\to I} = 0.5$, $\bar{g}_{AHP} = 0.2\ mS.cm^{-2}$, $\alpha_{AHP} = 0.001\ \mu M^{-1}.ms^{-1}$, $\beta_{AHP} = 0.002\ ms^{-1}$, $\gamma_{AHP} = 2$, $I_s = 0.03$.

Propagation condition model

We evaluated conditions for propagation of a pack of activity between neurons along the trajectory. Basically, propagation requires that, on average, spiking at frequency f in (upstream) presynaptic neurons must induce spiking at a frequency superior or equal to f in (down-stream) postsynaptic neurons. Therefore, we wrote a set of equations where presynaptic AMPA and NMDA input currents to a postsynaptic neuron are scaled by the firing frequency f of the presynaptic neuron and searched for frequency conditions where postsynaptic neurons fire at a frequency greater or equal than f. This *propagation condition*

model is an extremely simplified one-dimensional reduced representation of pack propagation within the local cortical recurrent network. This model is space-free and shall be considered as a representation of internal dynamics within the pack during its propagation, i.e. in a referential moving at the speed of pack propagation. Noticeably, the propagation condition model only considers a pre-/postsynaptic feedforward interaction, but does not take into account possible recurrent effects of the postsynaptic neuron on the presynaptic neurons or on the network. The propagation condition model nevertheless considers incoming excitatory and fixed inhibitory inputs from the entire network onto the postsynaptic neuron. These inputs are lumped together into common AMPA, NMDA and GABA-A terms that are quantitatively fitted on average synaptic currents impinging pack neurons in network simulations. The additional assumption is made that excitatory currents are essentially provided by upstream neurons within the pack (vs from neurons outside the pack, whether inside or outside the trajectory), so that AMPA and NMDA currents are scaled by f.

To tract the problem in a deterministic way, we leveraged from the observation that, regardless of whether neurons spike in the spontaneous regime or within the pack, 1) ISIs generally terminate through rapid final depolarizing fluctuations, due to chaotic dynamics, and that 2) these fluctuations start $\Delta t_{fluct}\sim 15ms$ before spiking. We numerically determined, from all ISIs during pack activity in network simulations, the mean time-to-spiking $\Delta t_{spiking}(V, f)$, as a function of the membrane potential and the firing frequency of the current ISI. We found that $\Delta t_{spiking}(V, f) = \Delta t_{fluct}$ was largely independent of firing frequency, which allowed to numerically estimate V_S' (around -53 mV).

We also considered, based on neuronal dynamics in the network model, that the membrane potential was essentially deterministically driven – before reaching V_S' and the final fluctuation to spiking – by average input and leak currents. Thus the membrane potential converged exponentially to its steady state V^* with

$$V(t) = V^*(f) + (V_R - V^*(f))exp\,(-t/\tau_m(f)),$$

where $V^*(f)$ was obtained from the equilibrium of ionic currents at steady-state

$$\bar{g}_{AMPA}\alpha_{fg}f(V^* - V_{AMPA}) + \bar{g}_{NMDA}\alpha_{fg}fm(V')(V^* - V_{NMDA}) + \bar{g}_{GABA-A}(V^* - V_{GABA-A}) + \bar{g}_L(V^* - V_L) + \bar{g}_{AMPA,FF}(V^* - V_{AMPA,FF})) = O,$$

with α_{fg} a conversion factor for dimensional compatibility and the non-linearity of the NMDA approximated to its value V', such that one can solve explicitly in terms of V^*:

$$V^*(f) = \frac{I}{g}(1 + \frac{g_{AN}}{g}f)^{-1},$$

with

$$I = \bar{g}_L V_L + \bar{g}_{GABA-A}V_{GABA-A},$$

$$g = \bar{g}_L + \bar{g}_{GABA-A} + \bar{g}_{AMPA,FF},$$

and

$$g_{AN} = \alpha_{fg}(\bar{g}_{AMPA} + \bar{g}_{NMDA})$$

which could be linearized ($\frac{g_{AN}}{g}f \ll 1$) to

$$V^*(f) = \frac{I}{g}(1 - \frac{g_{AN}}{g}f),$$

the membrane time-constant being written

$$\tau_m(f) = \frac{C}{\bar{g}_{AMPA}\alpha_{fg}f + \bar{g}_{NMDA}\alpha_{fg}fm(V') + \bar{g}_{GABA-A} + \bar{g}_L + \bar{g}_{AMPA,FF}},$$

and

$$\bar{g}_{AMPA} = \frac{I_{AMPA}^{Pack}}{\alpha_{fg}f_{pack}(\langle V^{Pack}\rangle - V_{AMPA})},$$

$$\bar{g}_{NMDA} = \frac{I_{NMDA}^{Pack}}{\alpha_{fg} f_{pack}(\langle V^{Pack}\rangle - V_{NMDA})},$$

$$\bar{g}_{GABA-A} = \frac{I_{GABA-A}^{Pack}}{(\langle V^{Pack}\rangle - V_{GABA-A})},$$

$$\bar{g}_{L} = \frac{I_{L}^{Pack}}{(\langle V^{Pack}\rangle - V_{L})},$$

$$\bar{g}_{AMPA,FF} = \frac{I_{AMPA-FF}^{Pack}}{(\langle V^{Pack}\rangle - V_{AMPA-FF})},$$

being estimated from pack mean membrane potential $\langle V^{Pack}\rangle$, mean currents (see below) and mean firing frequency f_{pack} obtained from network simulations.

As a final step of the propagation condition model, we then computed:

$$\Delta V(f) = V\left(t = \frac{1}{f}\right) - V_S' = V^*(f) + (V_R - V^*(f))exp\,(-f^{-1}\tau_m(f)^{-1}) - V_S'.$$

A negative $\Delta V(f)$ indicates that the potential has not yet reached, at time $T = \frac{1}{f}$, the threshold V_S' yielding rapid fluctuation-driven spiking so that postsynaptic frequency is lower than f, the presynaptic firing frequency. Therefore, propagation will fail. Conversely, a positive $\Delta V(f)$ indicates that the postsynaptic frequency exceeded the presynaptic one, so that propagation continues downstream. Finding a critical frequency f_θ such that $\Delta V(f_\theta) = 0$ indicates that pre- and postsynaptic frequencies are equal and propagation of spiking occurs at frequency f_θ. Moreover, the slope of $\Delta V(f)$ at f_θ determines the stability of the propagation. A negative slope indicates a stable propagation at frequency f_θ as fluctuations (due to chaotic network dynamics) will be quenched out by restoring forces driving the frequency back to f_θ (frequency increases below f_θ ($\Delta V(f) > 0$) and decreases above it ($\Delta V(f) < 0$)). A positive slope, to the contrary, indicates an unstable propagation with firing frequency ineluctably diverging from f_θ.

Computing the model indicated that, under our simplifying hypotheses, a single critical frequency f_θ was found at which the slope of the $\Delta V(f)$ was positive (see Results).

Therefore, the propagation condition model suggested that f_θ corresponded to an unstable fixed-point in the frequency dimension, acting as a threshold that separated, for trajectory neurons, the spontaneous regime (no pack propagation) from the regime of pack propagation. Actually, the propagation condition model predicted the value of f_θ quite well (see *Results*), with a value very close to that directly estimated from network simulations (see below). The quality of the propagation condition model was also evaluated by computing mean currents and comparing them to those found in network simulations (see *Results*). Currents were computed as:

$$I_{AMPA}(f) = \bar{g}_{AMPA}\alpha_{fg}f(\langle V\rangle(f) - V_{AMPA}),$$

$$I_{NMDA(f)} = \bar{g}_{NMDA}\alpha_{fg}f(\langle V\rangle(f) - V_{NMDA}),$$

$$I_{GABA-A}(f) = \bar{g}_{GABA-A}(\langle V\rangle(f) - V_{GABA-A}),$$

$$I_L(f) = \bar{g}_L(\langle V\rangle(f) - V_L),$$

$$I_{AMPA-FF(f)} = \bar{g}_{AMPA,FF}(\langle V\rangle(f) - V_{AMPA-FF}),$$

where

$$\langle V\rangle(f) = V^*(f) - f\tau_m(f)(V_R - V^*(f))(exp\,(-f^{-1}\tau_m(f)^{-1}) - 1)$$

Regime transition model

Although f_θ and the average currents (see *Results*) underlying the propagation condition were estimated, the model was however unable to identify the two stable frequency fixed-points $f_{non-pack}$ and f_{pack} setting the average spiking frequency in the spontaneous regime and during pack propagation in network simulations. This was because the simplifications regarding recurrent interactions within the network between excitatory neurons within the pack and neurons outside the pack (i.e. excitatory neurons inside and outside the trajectory, and inhibitory neurons) were too strong to account for the non-linearity ensuring negative feedbacks in the vicinity of $f_{non-pack}$ and f_{pack} stable fixed-points.

However, to better understand propagation of the pack within the network, we considered the co-existence of the unstable f_θ fixed-point and of the two stable $f_{non-pack}$ and f_{pack} stable fixed-points to build a phenomenological one-dimensional reduced *regime transition* model. Moreover, to evaluate the ability of this simplified model in explaining complex propagation behavior in the whole network by a simple model based on an unstable fixed-point separating two spontaneous and pack propagation regimes, we included a stochastic component and determined to which extent the simplified propagation model was able to account for transition rates between the spontaneous and propagation regimes in trajectory neurons. Specifically, the probability of the emergence of propagating packs from the spontaneous regime, $p(Spont.)$, the probability of propagating evoked packs $p(Evoked)$ and their duration were computed from the model.

In the model, the firing frequency of neurons within the trajectory followed:

$$\frac{df}{dt} = -\alpha_f(f - f_{non-pack})(f - f_\theta)\big(f - f_{pack}\big)/\tau_f + \sigma_f\sqrt{dt}x(t)$$

were α_f is a scaling factor, τ_f=$\tau_m(f_\theta)$ (see above), $x(t)$ is a Gaussian stochastic variable with mean 0 and standard deviation 1 and $\sigma_f = \sigma_{non-pack}$ for $f < f_{criterion}$ and $\sigma_f = \sigma_{pack}$ for $f \geq f_{criterion}$ with $\sigma_{non-pack}$ and σ_{pack} estimated from network simulations. The empirical estimation of f_θ in the network model was obtained by finding the frequency best separating pack and non-pack frequency distributions (see above).

Parameters

$\alpha_{fg} = 1mS.cm^{-2}.Hz^{-1}$, $V_S' = -53.05\ mV$, $\langle V^{pack}\rangle = -53.23mV$, $f_{non-pack} = 6.48\ Hz$, $f_{pack} = 14.34\ Hz$, $f_\theta = 9.7\ Hz$, $\alpha_f = 1e-3\ s^2$, $\sigma_{non-pack} = 1.96\ Hz$, $\sigma_{pack} = 3.55\ Hz$.

References for the Methods

1. Fujisawa, S., Amarasingham, A., Harrison, M. T. & Buzsáki, G. Behavior-dependent short-term assembly dynamics in the medial prefrontal cortex. *Nat. Neurosci.* **11**, 823–833 (2008).
2. Harvey, C. D., Coen, P. & Tank, D. W. Choice-specific sequences in parietal cortex during a virtual-navigation decision task. *Nature* **484**, 62–68 (2012).
3. Hussar, C. R. & Pasternak, T. Memory-Guided Sensory Comparisons in the Prefrontal Cortex: Contribution of Putative Pyramidal Cells and Interneurons. *J. Neurosci.* **32**, 2747–2761 (2012).
4. Pfeiffer, B. E. & Foster, D. J. Hippocampal place-cell sequences depict future paths to remembered goals. *Nature* **497**, 74–79 (2013).
5. Yang, S.-T., Shi, Y., Wang, Q., Peng, J.-Y. & Li, B.-M. Neuronal representation of working memory in the medial prefrontal cortex of rats. *Mol. Brain* **7**, 61 (2014).
6. Rikhye, R. V., Gilra, A. & Halassa, M. M. Thalamic regulation of switching between cortical representations enables cognitive flexibility. *Nat. Neurosci.* **21**, 1753–1763 (2018).
7. Diba, K. & Buzsáki, G. Forward and reverse hippocampal place-cell sequences during ripples. *Nat. Neurosci.* **10**, 1241–1242 (2007).
8. Jadhav, S. P., Rothschild, G., Roumis, D. K. & Frank, L. M. Coordinated Excitation and Inhibition of Prefrontal Ensembles during Awake Hippocampal Sharp-Wave Ripple Events. *Neuron* **90**, 113–127 (2016).
9. Kaefer, K., Nardin, M., Blahna, K. & Csicsvari, J. Replay of Behavioral Sequences in the Medial Prefrontal Cortex during Rule Switching. *Neuron* (2020) doi:10.1016/j.neuron.2020.01.015.
10. Chenkov, N., Sprekeler, H. & Kempter, R. Memory replay in balanced recurrent networks. *PLoS Comput. Biol.* **13**, (2017).
11. Pereira, U. & Brunel, N. Unsupervised Learning of Persistent and Sequential Activity. *Front. Comput. Neurosci.* **13**, (2020).
12. Sussillo, D. & Abbott, L. F. Generating Coherent Patterns of Activity from Chaotic Neural Networks. *Neuron* **63**, 544–557 (2009).
13. Laje, R. & Buonomano, D. V. Robust timing and motor patterns by taming chaos in recurrent neural networks. *Nat. Neurosci.* **16**, 925–933 (2013).
14. Xue, X., Halassa, M. M. & Chen, Z. S. Spiking recurrent neural networks represent task-relevant neural sequences in rule-dependent computation. *bioRxiv* 2021.01.21.427464 (2021) doi:10.1101/2021.01.21.427464.
15. Bi, G. Q. & Poo, M. M. Synaptic modifications in cultured hippocampal neurons: dependence on spike timing, synaptic strength, and postsynaptic cell type. *J. Neurosci. Off. J. Soc. Neurosci.* **18**, 10464–10472 (1998).
16. Hayashi, H. & Igarashi, J. LTD windows of the STDP learning rule and synaptic connections having a large transmission delay enable robust sequence learning amid background noise. *Cogn. Neurodyn.* **3**, 119–130 (2009).
17. Clopath, C., Büsing, L., Vasilaki, E. & Gerstner, W. Connectivity reflects coding: a model of voltage-based STDP with homeostasis. *Nat. Neurosci.* **13**, 344–352 (2010).
18. Boudewijns, Z. S. R. M. *et al.* Layer-specific high-frequency action potential spiking in the prefrontal cortex of awake rats. *Front. Cell. Neurosci.* **7**, (2013).
19. Compte, A. Temporally Irregular Mnemonic Persistent Activity in Prefrontal Neurons of Monkeys During a Delayed Response Task. *J. Neurophysiol.* **90**, 3441–3454 (2003).

20. Tchumatchenko, T., Geisel, T., Volgushev, M. & Wolf, F. Signatures of synchrony in pairwise count correlations. *Front. Comput. Neurosci.* **4**, (2010).
21. Brunel, N. Dynamics of Sparsely Connected Networks of Excitatory and Inhibitory Spiking Neurons. *J. Comput. Neurosci.* **8**, 183–208 (2000).
22. Poulet, J. F. A. & Petersen, C. C. H. Internal brain state regulates membrane potential synchrony in barrel cortex of behaving mice. *Nature* **454**, 881–885 (2008).
23. London, M., Roth, A., Beeren, L., Häusser, M. & Latham, P. E. Sensitivity to perturbations in vivo implies high noise and suggests rate coding in cortex. *Nature* **466**, 123–127 (2010).
24. Xue, M., Atallah, B. V. & Scanziani, M. Equalizing excitation–inhibition ratios across visual cortical neurons. *Nature* **511**, 596–600 (2014).
25. Destexhe, A., Rudolph, M. & Paré, D. The high-conductance state of neocortical neurons *in vivo*. *Nat. Rev. Neurosci.* **4**, 739–751 (2003).
26. Turrigiano, G. G., Leslie, K. R., Desai, N. S., Rutherford, L. C. & Nelson, S. B. Activity-dependent scaling of quantal amplitude in neocortical neurons. *Nature* **391**, 892–896 (1998).
27. Abbott, L. F. & Nelson, S. B. Synaptic plasticity: taming the beast. *Nat. Neurosci.* **3**, 1178–1183 (2000).
28. Sarazin, M. X. B., Victor, J., Medernach, D., Naudé, J. & Delord, B. Online Learning and Memory of Neural Trajectory Replays for Prefrontal Persistent and Dynamic Representations in the Irregular Asynchronous State. *Front. Neural Circuits* **0**, (2021).
29. Rodriguez, G. *et al.* Conditional bistability, a generic cellular mnemonic mechanism for robust and flexible working memory computations. *J. Neurosci.* 1992–17 (2018) doi:10.1523/JNEUROSCI.1992-17.2017.
30. Zhang, J.-C., Lau, P.-M. & Bi, G.-Q. Gain in sensitivity and loss in temporal contrast of STDP by dopaminergic modulation at hippocampal synapses. *Proc. Natl. Acad. Sci.* **106**, 13028–13033 (2009).
31. Batuev, A. S. Two neuronal systems involved in short-term spatial memory in monkeys. *Acta Neurobiol. Exp. (Warsz.)* **54**, 335–344 (1994).
32. Schmitt, L. I. *et al.* Thalamic amplification of cortical connectivity sustains attentional control. *Nature* **545**, 219–223 (2017).
33. Liu, J. K. & Buonomano, D. V. Embedding Multiple Trajectories in Simulated Recurrent Neural Networks in a Self-Organizing Manner. *J. Neurosci.* **29**, 13172–13181 (2009).
34. Fiete, I. R., Senn, W., Wang, C. Z. H. & Hahnloser, R. H. R. Spike-Time-Dependent Plasticity and Heterosynaptic Competition Organize Networks to Produce Long Scale-Free Sequences of Neural Activity. *Neuron* **65**, 563–576 (2010).
35. Saxe, A., Nelli, S. & Summerfield, C. If deep learning is the answer, what is the question? *Nat. Rev. Neurosci.* **22**, 55–67 (2021).
36. Wang, X.-J. Synaptic Basis of Cortical Persistent Activity: the Importance of NMDA Receptors to Working Memory. *J. Neurosci.* **19**, 9587–9603 (1999).
37. Rolls, E. T. & Deco, G. A computational neuroscience approach to schizophrenia and its onset. *Neurosci. Biobehav. Rev.* **35**, 1644–1653 (2011).
38. Mehring, C., Hehl, U., Kubo, M., Diesmann, M. & Aertsen, A. Activity dynamics and propagation of synchronous spiking in locally connected random networks. *Biol. Cybern.* **88**, 395–408 (2003).
39. Seeholzer, A., Deger, M. & Gerstner, W. Stability of working memory in continuous attractor networks under the control of short-term plasticity. *PLOS Comput. Biol.* **15**, e1006928 (2019).

40. Lee, A. K. & Wilson, M. A. Memory of Sequential Experience in the Hippocampus during Slow Wave Sleep. *Neuron* **36**, 1183–1194 (2002).
41. Euston, D. R., Tatsuno, M. & McNaughton, B. L. Fast-Forward Playback of Recent Memory Sequences in Prefrontal Cortex During Sleep. *Science* **318**, 1147–1150 (2007).
42. Girardeau, G., Benchenane, K., Wiener, S. I., Buzsáki, G. & Zugaro, M. B. Selective suppression of hippocampal ripples impairs spatial memory. *Nat. Neurosci.* **12**, 1222–1223 (2009).
43. Buzsáki, G. & Moser, E. I. Memory, navigation and theta rhythm in the hippocampal-entorhinal system. *Nat. Neurosci.* **16**, 130–138 (2013).
44. Durstewitz, D. & Deco, G. Computational significance of transient dynamics in cortical networks. *Eur. J. Neurosci.* **27**, 217–227 (2008).
45. Sreenivasan, K. K., Curtis, C. E. & D'Esposito, M. Revisiting the role of persistent neural activity during working memory. *Trends Cogn. Sci.* **18**, 82–89 (2014).
46. Mello, G. B. M., Soares, S. & Paton, J. J. A Scalable Population Code for Time in the Striatum. *Curr. Biol.* **25**, 1113–1122 (2015).
47. Bolkan, S. S. *et al.* Thalamic projections sustain prefrontal activity during working memory maintenance. *Nat. Neurosci.* **20**, 987–996 (2017).
48. Spaak, E., Watanabe, K., Funahashi, S. & Stokes, M. G. Stable and Dynamic Coding for Working Memory in Primate Prefrontal Cortex. *J. Neurosci.* **37**, 6503–6516 (2017).
49. Pastalkova, E., Itskov, V., Amarasingham, A. & Buzsaki, G. Internally Generated Cell Assembly Sequences in the Rat Hippocampus. *Science* **321**, 1322–1327 (2008).
50. Cromer, J. A., Roy, J. E. & Miller, E. K. Representation of Multiple, Independent Categories in the Primate Prefrontal Cortex. *Neuron* **66**, 796–807 (2010).
51. Dale, H. Pharmacology and Nerve-endings (Walter Ernest Dixon Memorial Lecture): (Section of Therapeutics and Pharmacology). *Proc. R. Soc. Med.* **28**, 319–332 (1935).
52. Beaulieu, C., Kisvarday, Z., Somogyi, P., Cynader, M. & Cowey, A. Quantitative distribution of gaba-immunopositive and -immunonegative neurons and synapses in the monkey striate cortex (area 17). *Cereb. Cortex* **2**, 295–309 (1992).
53. Thomson, A. M. Synaptic Connections and Small Circuits Involving Excitatory and Inhibitory Neurons in Layers 2-5 of Adult Rat and Cat Neocortex: Triple Intracellular Recordings and Biocytin Labelling In Vitro. *Cereb. Cortex* **12**, 936–953 (2002).
54. Song, S., Sjöström, P. J., Reigl, M., Nelson, S. & Chklovskii, D. B. Highly Nonrandom Features of Synaptic Connectivity in Local Cortical Circuits. *PLOS Biol.* **3**, e68 (2005).
55. Haj-Dahmane, S. & Andrade, R. Calcium-Activated Cation Nonselective Current Contributes to the Fast Afterdepolarization in Rat Prefrontal Cortex Neurons. *J. Neurophysiol.* **78**, 1983–1989 (1997).
56. Villalobos, C., Shakkottai, V. G., Chandy, K. G., Michelhaugh, S. K. & Andrade, R. SKCa Channels Mediate the Medium But Not the Slow Calcium-Activated Afterhyperpolarization in Cortical Neurons. *J. Neurosci.* **24**, 3537–3542 (2004).
57. Faber, E. L. & Sah, P. Functions of Sk Channels in Central Neurons. *Clin. Exp. Pharmacol. Physiol.* **34**, 1077–1083 (2007).
58. Brunel, N. & Wang, X. J. Effects of neuromodulation in a cortical network model of object working memory dominated by recurrent inhibition. *J. Comput. Neurosci.* **11**, 63–85 (2001).
59. Jahr, C. E. & Stevens, C. F. Voltage dependence of NMDA-activated macroscopic conductances predicted by single-channel kinetics. *J. Neurosci.* **10**, 3178–3182 (1990).
60. Wang, H., Stradtman, G. G., Wang, X.-J. & Gao, W.-J. A specialized NMDA receptor

function in layer 5 recurrent microcircuitry of the adult rat prefrontal cortex. *Proc. Natl. Acad. Sci.* (2008) doi:10.1073/pnas.0804318105.
61. Destexhe, A., Mainen, Z. F. & Sejnowski, T. J. Kinetic models of synaptic transmission. *Methods Neuronal Model.* **2**, 1–25 (1998).
62. Wolf, A., Swift, J., Swinney, H. & Vastano, J. Determining Lyapunov exponents from a time series. *Phys. Nonlinear Phenom.* 285–317 (1985).
63. Huffaker, R. Phase Space Reconstruction from Econommic Time Series Data: Improving Models of Complex Real-World Dynamic Systems. *Int. J. Food Syst. Dyn.* **1**, 184–193 (2010).
64. Kliková, B. & Raidl, A. Reconstruction of Phase Space of Dynamical Systems Using Method of Time Delay. *Proc. 20th Annu. Conf. Dr. Stud. - WDS 2011* 83–87 (2011).
65. Kantz, H. & Schreiber, T. *Nonlinear Time Series Analysis*. (Cambridge University Press, 2004).
66. Kennel, M. B., Brown, R. & Abarbanel, H. D. I. Determining embedding dimension for phase-space reconstruction using a geometrical construction. *Phys. Rev. A* **45**, 3403–3411 (1992).
67. Hegger, R. & Kantz, H. Improved false nearest neighbor method to detect determinism in time series data. *Phys. Rev. E Stat. Phys. Plasmas Fluids Relat. Interdiscip. Top.* **60**, 4970–4973 (1999).
68. Shinomoto, S., Miyazaki, Y., Tamura, H. & Fujita, I. Regional and Laminar Differences in In Vivo Firing Patterns of Primate Cortical Neurons. *J. Neurophysiol.* **94**, 567–575 (2005).
69. Golomb, D., Hansel, D. & Mato, G. Chapter 21 Mechanisms of synchrony of neural activity in large networks. in *Handbook of Biological Physics* (eds. Moss, F. & Gielen, S.) vol. 4 887–968 (North-Holland, 2001).